Voyager 2 at Neptune: Imaging Science Results

B. A. SMITH, L. A. SODERBLOM, D. BANFIELD, C. BARNET, A. T. BASILEVKSY, R. F. BEEBE, K. BOLLINGER, J. M. BOYCE, A. BRAHIC, G. A. BRIGGS, R. H. BROWN, C. CHYBA, S. A. COLLINS, T. COLVIN, A. F. COOK II, D. CRISP, S. K. CROFT, D. CRUIKSHANK, J. N. CUZZI, G. E. DANIELSON, M. E. DAVIES, E. DE JONG, L. DONES, D. GODFREY, J. GOGUEN, I. GRENIER, V. R. HAEMMERLE, H. HAMMEL, C. J. HANSEN, C. P. HELFENSTEIN, C. HOWELL, G. E. HUNT, A. P. INGERSOLL, T. V. JOHNSON, J. KARGEL, R. KIRK, D. I. KUEHN, S. LIMAYE, H. MASURSKY, A. MCEWEN, D. MORRISON, T. OWEN, W. OWEN, J. B. POLLACK, C. C. PORCO, K. RAGES, P. ROGERS, D. RUDY, C. SAGAN, J. SCHWARTZ, E. M. SHOEMAKER, M. SHOWALTER, B. SICARDY, D. SIMONELLI, J. SPENCER, L. A. SROMOVSKY, C. STOKER, R. G. STROM, V. E. SUOMI, S. P. SYNOTT, R. J. TERRILE, P. THOMAS, W. R. THOMPSON, A. VERBISCER, J. VEVERKA

Voyager 2 images of Neptune reveal a windy planet characterized by bright clouds of methane ice suspended in an exceptionally clear atmosphere above a lower deck of hydrogen sulfide or ammonia ices. Neptune's atmosphere is dominated by a large anticyclonic storm system that has been named the Great Dark Spot (GDS). About the same size as Earth in extent, the GDS bears both many similarities and some differences to the Great Red Spot of Jupiter. Neptune's zonal wind profile is remarkably similar to that of Uranus. Neptune has three major rings at radii of 42,000, 53,000, and 63,000 kilometers. The outer ring contains three higher density arc-like segments that were apparently responsible for most of the ground-based occultation events observed during the current decade. Like the rings of Uranus, the Neptune rings are composed of very dark material; unlike that of Uranus, the Neptune system is very dusty. Six new regular satellites were found, with dark surfaces and radii ranging from 200 to 25 kilometers. All lie inside the orbit of Triton and the inner four are located within the ring system. Triton is seen to be a differentiated body, with a radius of 1350 kilometers and a density of 2.1 grams per cubic centimeter; it exhibits clear evidence of early episodes of surface melting. A now rigid crust of what is probably water ice is overlain with a brilliant coating of nitrogen frost, slightly darkened and reddened with organic polymer material. Streaks of organic polymer suggest seasonal winds strong enough to move particles of micrometer size or larger, once they become airborne. At least two active plumes were seen, carrying dark material 8 kilometers above the surface before being transported downstream by high level winds. The plumes may be driven by solar heating and the subsequent violent vaporization of subsurface nitrogen.

VOYAGER 2 ACQUIRED MORE THAN 9000 images of Neptune, its rings, and its satellites during a 6-month interval surrounding the spacecraft's closest approach to the planet on 25 August 1989. The combination of the very low light levels experienced at Neptune [30 astronomical units (AU) from the sun] and the low albedo of its rings and inner satellites, however, made it necessary to employ uncomfortably long exposure times for many of the sequences. This, in turn, required the use of a special sequence design to compensate for image smear caused by spacecraft motion. In addition, spacecraft engineering teams modified the attitude control software to provide further reduction of random spacecraft motion over that achieved earlier at the Uranus encounter (*1*). The success of these techniques is aptly demonstrated in the striking photographs that Voyager 2 has sent back to Earth from the very edge of our planetary system.

B. A. Smith, S. K. Croft, V. R. Haemmerle, J. Kargel, C. C. Porco, R. G. Strom, University of Arizona, Tucson, AZ 85721.
L. A. Soderblom, R. Kirk, H. Masursky, A. McEwen, E. M. Shoemaker, U.S. G.S., Flagstaff, AZ 86001.
D. Banfield, G. E. Danielson, E. De Jong, C. Howell, A. P. Ingersoll, J. Schwartz, California Institute of Technology, Pasadena, CA 91125.
C. Barnet, R. F. Beebe, D. I. Kuehn, New Mexico State University, Las Cruces, NM 88003.
A. T. Basilevsky, Vernadsky Institute for Cosmochemistry, USSR Academy of Science, Moscow.
K. Bollinger, R. H. Brown, S. A. Collins, D. Crisp, J. Goguen, H. Hammel, C. J. Hansen, T. V. Johnson, W. Owen, D. Rudy, S. P. Synnott, R. J. Terrile, Jet Propulsion Laboratory, Pasadena, CA 91109.
J. M. Boyce and G. A. Briggs, NASA Headquarters, Washington, DC 20546.
A. Brahic, I. Grenier, B. Sicardy, Observatoire de Paris, Meudon, Paris, France.
C. Chyba, C. P. Helfenstein, C. Sagan, D. Simonelli, P. Thomas, W. R. Thompson, A. Verbiscer, J. Veverka, Cornell University, Ithaca, NY 14853.
A. F. Cook II, Center for Astrophysics, Cambridge, MA 02138.
T. Colvin and M. E. Davies, P. Rogers, Rand Corporation, Santa Monica, CA 90406.
D. Cruikshank, J. N. Cuzzi, D. Morrison, J. B. Pollack, C. Stoker, NASA Ames Research Center, Moffett Field, CA 94035.
L. Dones, University of Toronto, Toronto, Ontario M5S 1A1, Canada.
D. Godfrey, National Optical Astronomy Observatories, Tucson, AZ 85726.
G. E. Hunt, Logica International, Ltd., 64 Neisman Street, London, England W1A 4SE.
S. Limaye, L. A. Sromovsky, V. E. Suomi, University of Wisconsin, Madison, WI 53706.
T. Owen, State University of New York, Stony Brook, NY 11794.
K. Rages, Mycol, Inc., Sunnyvale, CA 94087.
M. Showalter, Stanford University, Stanford, CA 94305.
J. Spencer, Institute for Astronomy, University of Hawaii, Honolulu, HI 95822.

The Atmosphere of Neptune

Neptune's atmosphere provided many surprises during the Voyager encounter. The high wind speeds, the persistence of large oval storm systems, and the hour-to-hour variability of small-scale features were unexpected in an atmosphere that receives 1/20 as much energy (power per unit area) from internal heat and absorbed sunlight as Jupiter and only 1/350 as much energy as Earth. Large features near the equator move westward relative to the interior at speeds up to 325 m s^{-1}, making Neptune one of the windiest planets (with Saturn) in the solar system. Small-scale features appear to move at twice this speed. The Great Dark Spot (GDS), a weather system comparable to Earth in size, stretches and contracts as it rolls in a counterclockwise direction with a 16-day period. Bright clouds cast shadows on the main cloud deck 50 to 100 km below.

At some latitudes, the bright clouds resemble mountain lee waves, where large-scale patterns remain fixed while small-scale elements move through them. Such patterns were not seen on the other gas giant planets. Although the atmospheres of the giant planets do exhibit some common phenomena—colored clouds and hazes, latitudinal banding, strong winds, for example—there remain many differences and they do not follow obvious rules.

Discrete cloud features and banded structure. The largest discrete feature in Neptune's atmosphere is the GDS, which resembles Jupiter's Great Red Spot (GRS) in several respects. Neptune's GDS has an average extent of 38° and 15° in longitude and latitude, respectively (Figs. 1A, 2, and 3A), compared with 30° and 20° for the GRS (*2*). The GDS is located at about the same latitude as the GRS (20°S) and seems to have a similar anticyclonic circulation sense (counterclockwise in the southern hemisphere). Evidence for the anticyclonic rotation of the GDS is based primarily on visual impressions gained from a time-lapse sequence, rather than on direct measurement

Downloaded from on March 29, 2016

of the displacement of small features. However, there are significant differences between the GDS and the GRS. The circulation of the GRS modifies its surrounding environment, forming a turbulent-wake region to the west of the feature (*2*). Although the GDS on Neptune also appears to influence its immediate environment, the regions surrounding it appear morphologically more uniform compared to those on Jupiter. Furthermore, the GDS drifts rapidly westward at speeds over 300 m s^{-1} relative to the planetary radio rate (*3, 4*), while the GRS drifts westward at an average rate of only 3 m s^{-1} (*5*).

The bright companion along the southern edge of the GDS (Figs. 1 and 3A) was detected in January 1989; it was the first discrete feature observed on Neptune by Voyager 2, and was also seen in ground-based images (*4, 6*). This feature persistently appeared on the southern edge of the GDS, although its brightness and precise shape varied with time. In Fig. 3A, the bright companion is resolved into east-west linear structures.

Time-lapse images of the GDS and its vicinity (Fig. 4) suggest that the bright companion may be similar to orographic clouds observed on Earth, that is, clouds created by air being forced upward by the presence of a mountain. Specifically, the smallest features appeared to move relative to the structure as a whole. The role of topography, necessary for the formation of terrestrial orographic clouds, may be played by temperature and pressure anomalies associated with the GDS.

A bright feature near the southern pole (71°S) was first seen in April 1989 (Fig. 1B). This south polar feature (SPF) appears to be not one discrete feature but rather an active arc extending over some 90° of longitude and constrained to a latitudinal band spanning less than 5°. The intensity and distribution of brightness along this arc was seen to vary significantly during a single rotation of the planet.

The third bright feature discovered by Voyager (after the bright companion to the GDS and the SPF) was the "Scooter," a bright compact feature centered near 42°S (Fig. 1A); despite its name, however, it is not the fastest moving feature (*4*). The "Scooter" is composed of many small streaks stacked in latitude (Fig. 3C) rather than being a single round or oval storm system. The number and length of these streaks varies (causing the feature to change shape from round to square to triangular), but the composite structure identified as the "Scooter" persisted as a unit throughout the 80-day encounter period.

Soon after the discovery of the "Scooter," a second dark feature (D2) was identified in the southern hemisphere at a latitude of 55°S (Figs. 1, A and B). Several weeks after its discovery, a bright core developed at the center of the dark feature. The core remained visible for the remainder of the encounter, although its brightness varied. Small-scale cloud features were clearly visible within the bright core (Fig. 3B). Figure 5 shows three high-resolution images of the cloud structure in the core of D2. The size and shape of the local details varied on time scales of hours. On Jupiter, features similar to D2 rotate anticyclonically, but the sense of circulation has not yet been detected in D2.

Voyager images of Neptune's atmosphere (Fig. 1, A and B) revealed a banded zonal structure with the brightest region located near 20°S. Bands of lower reflectivity in the northern and southern hemispheres were located at 6°N to 25°N and 45°S to 70°S, that is, the brightness variation was not symmetrical about the equator. This asymmetry is also seen in Fig. 2, where the effect of viewing geometry was removed to show the brightness at normal incidence (*7*). Bright ephemeral streamers were seen both at the latitude of the GDS (Fig. 6) and at about 27°N. These streamers were highly variable in both time and brightness. Methane-band images of the southern hemi-

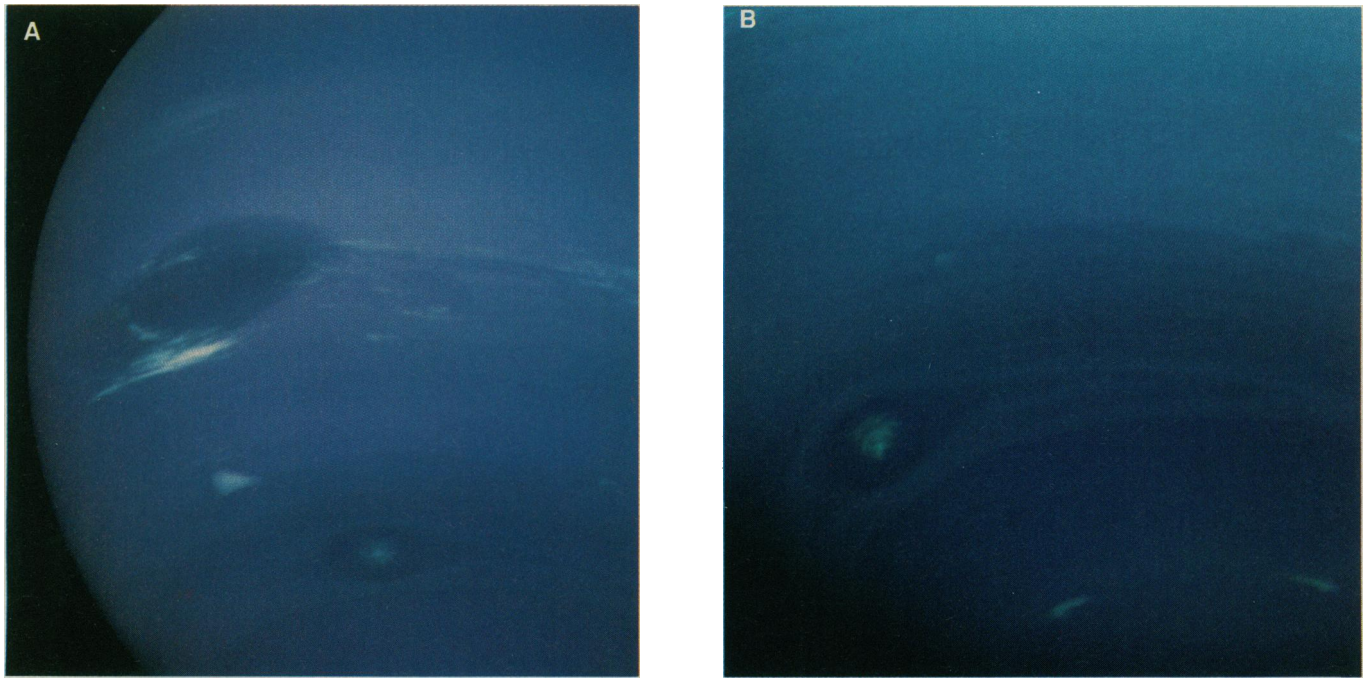

Fig. 1. Color images of Neptune, taken on 21.7 August 1989. These color images were reconstructed by combining images obtained through green and clear filters. North is up in all figures of Neptune except where explicitly noted otherwise. (**A**) The Great Dark Spot and its associated bright companion are visible, along with various bright streamers at the same latitude. The "Scooter" is the bright triangular feature south of the GDS. D2 (the second dark feature) is visible even further south. [Image processing by C. J. Levine] (**B**) This view focuses on the south polar region, showing the south polar feature and another view of D2. The south polar feature (SPF) is not a single discrete feature, but rather an arc of activity, extending about 90° in longitude and constrained to a latitudinal band less than 5° wide. Only the ends of the arc are bright in this image. This picture was obtained 14 hours after the first image.

sphere revealed a bright band within 15° of the south pole. To within an uncertainty of 1°, a small feature lies at the south rotational pole (Figs. 7 and 8). This structure suggests a well-organized polar circulation that has no analogue in the polar regions of the other giant planets.

Vertical structure from feature contrast. Analyses of ground-based observations of Neptune (*8–11*) and analogous studies of Uranus (*11, 12*) indicated the presence of three major particulate layers in the observable atmosphere of Neptune (Fig. 9). A photochemical smog layer was predicted at pressures starting at about 5 mbar in the lower stratosphere and extending to lower altitudes in the stratosphere and upper troposphere (*8, 10, 13*). This layer, composed of lower order hydrocarbons such as ethane, acetylene, and diacetylene, results from photochemistry of methane driven by solar ultraviolet radiation within the lower and upper stratosphere.

Two condensation cloud layers are thought to occur in the upper troposphere. Methane should begin condensing at about the 1.5-bar level (*8–10, 14*) while a more optically thick cloud appears to exist near the 3-bar level (*8–10*). This deeper cloud may be made of hydrogen sulfide ice particles (*8, 10*), but ammonia also is present (*14*).

The Voyager images provide both vertical and horizontal structural information (Fig. 1, A and B). We used several complementary approaches for estimating the absolute and relative heights of these features. In the first approach, we studied the wavelength dependence of the contrast of features. As shown in Figs. 8 and 10, the contrast of bright and dark features varies markedly with wavelength. For example, the "Scooter" displays the greatest contrast in the orange-filtered image and much lower contrast in both the UV and longer wavelength methane filter (designated MeJ, with center wavelength 619 nm). On the other hand, most other bright features, such as the bright companion to the Great Dark Spot, show an enhanced contrast in the MeJ band relative to orange. The Great Dark Spot has its maximum negative contrast in the blue filter.

We interpret the contrast variations in the following way: molecular Rayleigh scattering in the upper layers tends to mask deep-lying features at the shortest wavelengths (the Rayleigh scattering optical depth is about 5 above the 3-bar cloud in the UV filter), while absorption by gaseous methane tends to mask deep features in the methane filters (especially the MeJ filter). Thus, the cloud tops of the major bright features are not all located at the same altitude. In particular, the "Scooter" is situated at a much lower altitude than the bright companion of the GDS, as evidenced by the "Scooter's" decreasing contrast at methane-band wavelengths relative to blue. Further-

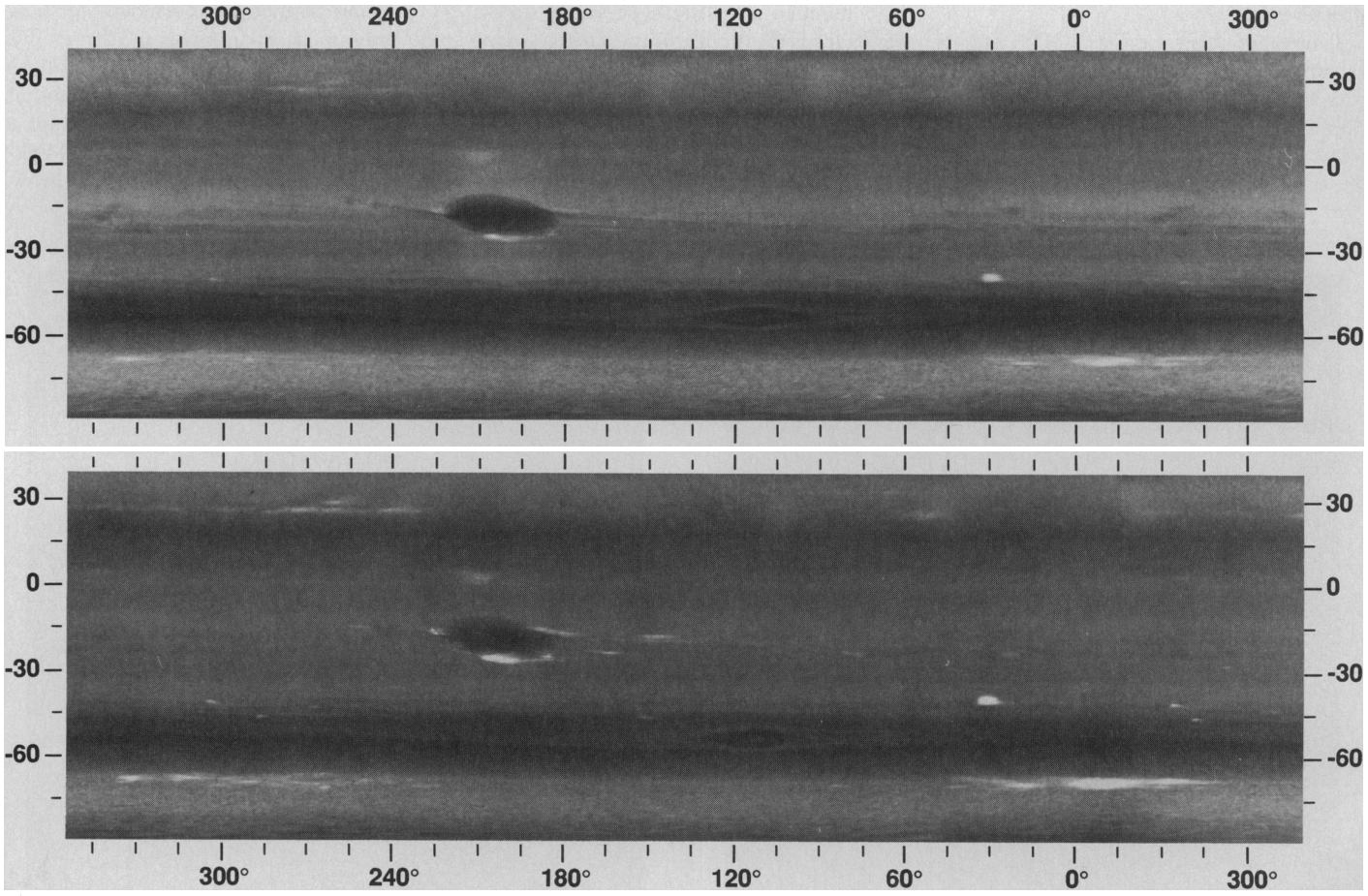

Fig. 2. Simple cylindrical projection mosaics of narrow-angle images taken through the blue (**top**) and green (**bottom**) filters on 17–18 August 1989. Latitude is planetocentric and longitude is based on a rotation period of 17 hours 52 min, the "predict" period used to plan Voyager observation sequences. This is longer than the 16.1 hour period derived from the Planetary Radio Astronomy investigation (*3*). For each mosaic, approximately ten images were shuttered, during which time the planet rotated through slightly more than one rotation. Thus features visible near the right edge of the mosaic appear one rotation later near the left edge. Differential rotation is evident near longitudes of 300° and latitudes of −41° (41°S) and −46° (46°S). Feature evolution is evident at +26° (26°N) and −68° (68°S). An inverse photometric function was applied to each image to reduce limb darkening. A digital filter was applied to the completed mosaics to reduce the contrast of the large-scale bands and bring out the small-scale features. [Image processing by J. R. Yoshimizu]

more, the "Scooter" must be located below the base of the methane cloud, because it is masked in the MeJ filter (assuming there is little methane above the base of the methane cloud). Preliminary radiative transfer calculations that approximately reproduce measured contrasts substantiate these conclusions (*8, 15*). The generally negative contrast of the GDS and the fact that its blue and MeJ contrasts are comparable might indicate that the atmosphere is relatively clear above the GDS; that is, the amount of scattering above the top of the 3-bar cloud is low (corresponding to a lower optical thickness of the methane cloud). If so, there is a gradual change from the outer to inner regions of the GDS, with the clearest atmosphere occurring toward its center. Alternatively, the negative contrast might indicate that the "3-bar" cloud is actually at a deeper level in the center of the GDS.

With the exception of the "Scooter," the discrete bright features are probably methane condensation clouds. These features are prominent, localized, and dynamically active. In contrast, a photochemically produced haze is likely to be spatially uniform and inactive. Such a haze layer is visible at the limb in the images taken through the MeJ and MeU filters (the latter with center wavelength 541 nm) (Fig. 6) and was inferred from ground-based observations of center-to-limb brightness profiles (*8*). In the troposphere, methane gas is probably abundant enough to produce a prominent localized cloud. The deep (labeled H_2S?) condensation cloud (Fig. 9) is not a candidate for features that are bright in the MeJ filter, because that cloud has too much absorbing methane gas above it to appear bright at this wavelength.

Figure 7 shows D2 and the SPF visible on Neptune's crescent in all filters from UV to orange. Such visibility of features on the crescents was not apparent at Jupiter, Saturn, or Uranus, and this is consistent with the idea that the bright white features on Neptune extend to considerable heights above most of the haze and atmospheric gases.

Vertical structure from limb scans and cloud shadows. Images obtained at high phase angles provide evidence for the existence of a stratospheric haze and also place constraints on its properties. Such images are particularly effective for detecting the presence of optically thin stratospheric hazes, since the submicronmeter-sized haze particles preferentially scatter sunlight at small scattering angles (large phase angles). Particle visibility is also enhanced by the long slant paths through the atmosphere that occur under these viewing conditions. Figure 11A shows several radial line scans across the planet's limb. The scans reach a nearly constant brightness at lower altitudes where the slant-path optical depth exceeds unity (or the vertical optical depth exceeds several hundredths).

On the basis of experience with similar images obtained at Uranus (*11*), we suspect that the transition to constant brightness (400 km relative alitude in Fig. 11A) occurs within the bottom scale height of the stratosphere (80 to 100 km altitude in Fig. 9). Light scattered by a combination of aerosols and gas molecules is detectable to altitudes above 550 km in Fig. 11A at least 150 km above the constant brightness portion. The sharp increase in brightness with decreasing altitude just above the constant brightness region indicates the existence of particles in this region of the stratosphere, since the brightness increases more rapidly than would be expected from molecular Rayleigh scattering alone. This point is further demonstrated in Fig. 11B, which shows an extinction profile derived by inverting one of the limb scans of Fig. 11A (*11, 13, 16*). The region with a rapid increase in the extinction coefficient may mark the altitude where temperatures become cold enough for gaseous ethane to condense into ice particles (*13*).

Cloud shadows provided additional data about vertical structure. As shown in Fig. 12, some discrete clouds that were observed

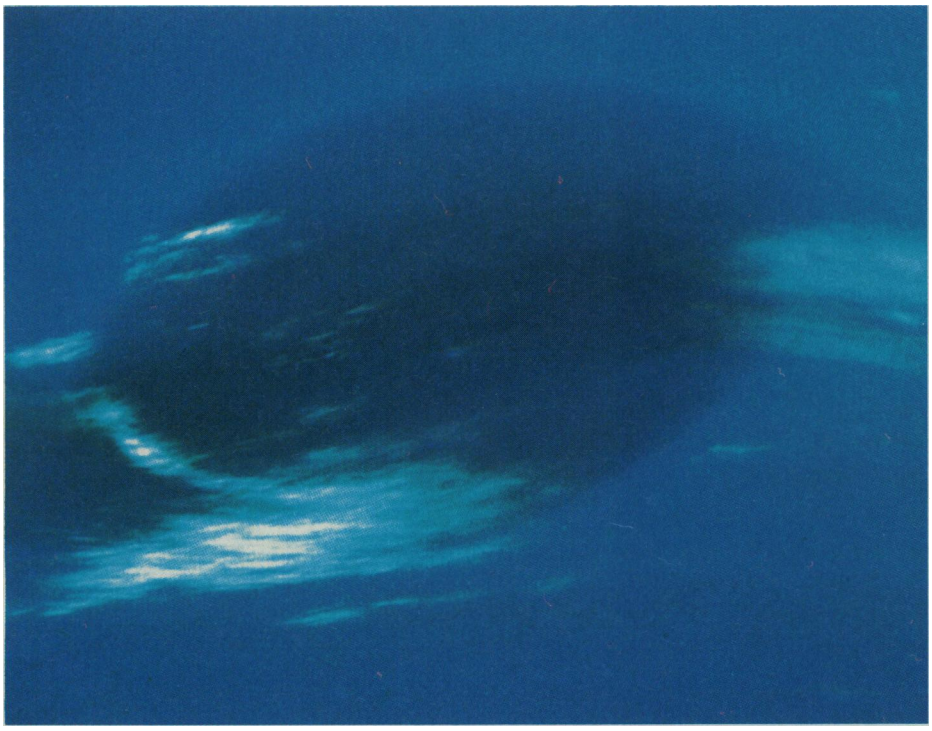

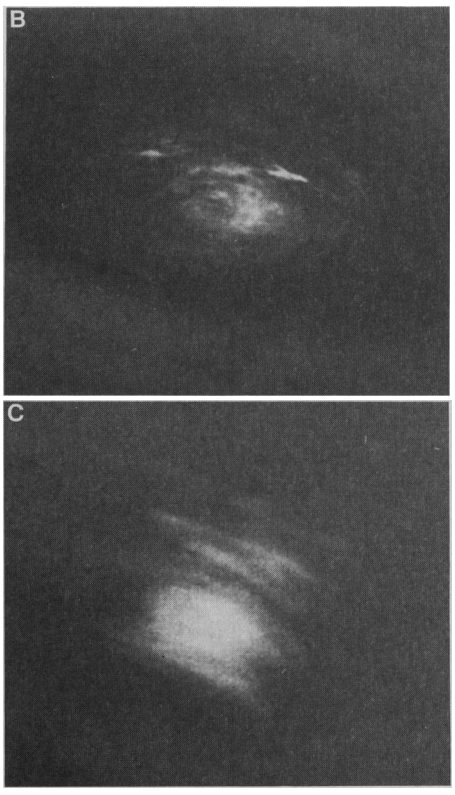

Fig. 3. High-resolution images of Neptune's largest discrete features. (**A**) In this high-resolution image of the GDS and its bright companion taken 45 hours before closest approach, the companion is resolved into many bright E-W linear streaks. [Image processing by C. L. Stanley] (**B**) Our highest resolution image of D2 was obtained during an IRIS observation on 24.4 August 1989. (**C**) This image taken on 23.3 August 1989 reveals the detailed structure of the "Scooter." It is composed of many bright streaks which vary on time scales of days, causing the "Scooter" to sometimes appear square or triangular (for example, see Fig. 1A).

when the sun was low on the horizon displayed a dark adjoining region. Although variable scattering geometries could cause such variations in brightness even if all parts of the cloud tops were directly illuminated by the sun, several factors suggest that these dark features are shadows cast by high clouds on a more uniform underlying cloud deck.

First, the features always appear in the direction away from the sun, relative to their associated bright feature. Second, the length of the dark features in the sun/anti-sun direction tends to increase with decreasing solar elevation angle. Third, the contrast of the dark regions with respect to the surrounding background tends to be much smaller in the violet filter than in longer wavelength filters (the contrast is only 20% in the green filter). We attribute this to a filling-in of the shadow by sunlight scattered by overlying gas molecules and aerosols, which preferentially scatter sunlight at the shorter wavelengths. Finally, in all cases, the clouds casting shadows appear markedly bright in MeJ images, implying that they are elevated relative to their surroundings.

We estimated the heights of the bright cloud features above the underlying cloud deck by taking brightness scans across them in the sun/anti-sun direction, measuring the distance between the anti-sunward edges of the shadow and its associated cloud, and applying appropriate geometrical relationships. Separate measurements of clouds and associated shadows shown in Fig. 12 yielded a mean height of about 100 km, with a dispersion of about 50 km. The latitude of this cloud field is about 27°N. At the temperature of the upper troposphere, the pressure scale height is about 20 km. If the underlying cloud deck is associated with the 3-bar cloud, then those individual clouds reach altitudes close to the tropopause and therefore could act as an important vehicle for the exchange of constituents, such as methane, between the troposphere and stratosphere.

We also made height estimates for clouds associated with the south polar feature at 71°S. These clouds attain an average elevation of about 50 km above the underlying cloud deck, about half that of the northern cloud field. The results of the shadow analy-

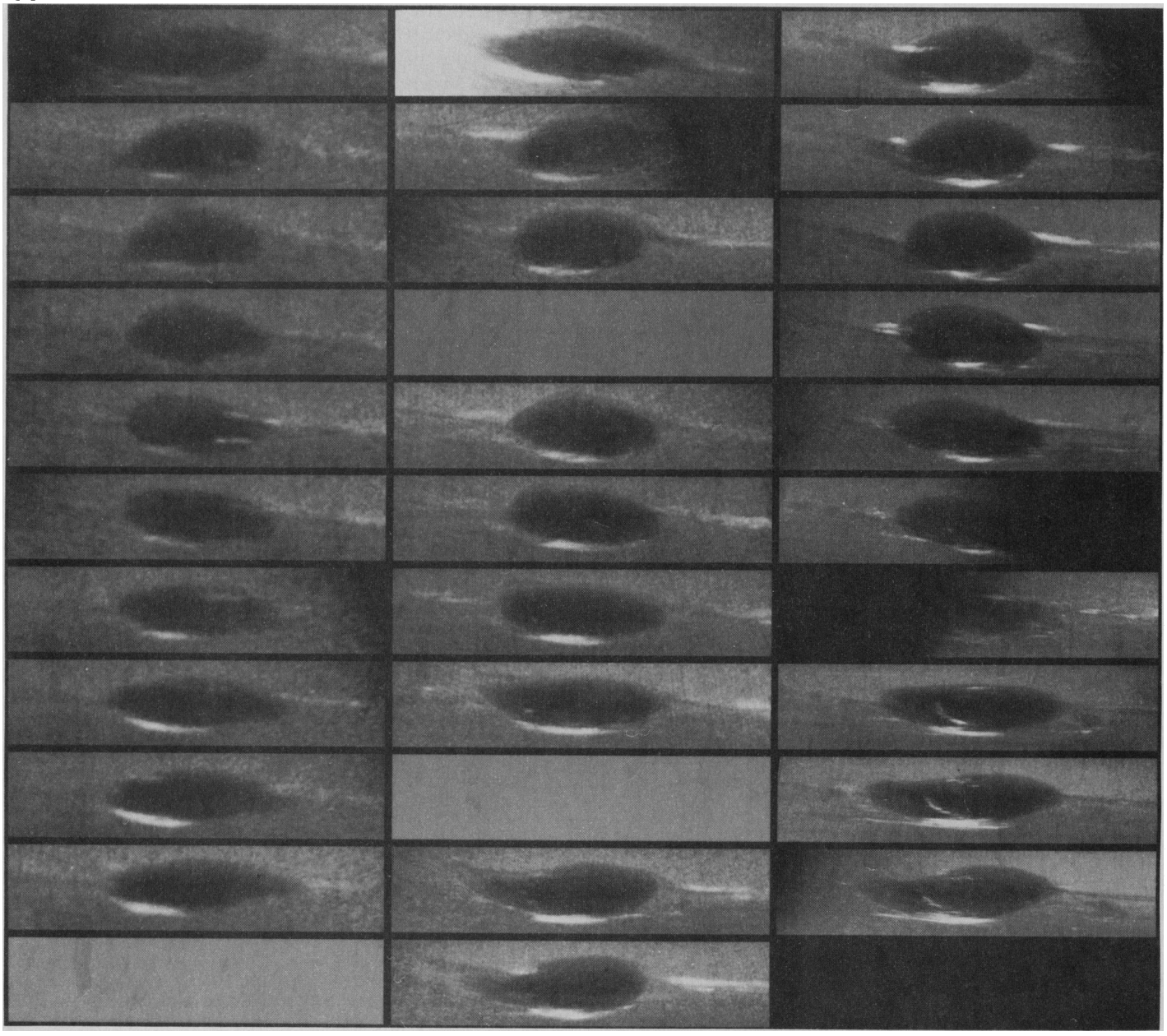

sis were consistent for observations made at both high and low phase angles (about 140 and 20 degrees, respectively), where the viewing geometry is quite different.

Large-scale variability of features. All of the larger-scale features tracked during observatory phase exhibited latitudinal drifting associated with changes of wind speed (*4*). D2 exhibited the largest change of wind speed. When first measured, it was located at 55°S and had a rotation period of 16.0 hours (Figs. 1 and 5). Then D2 drifted northward to 51°S, and its period increased to 16.3 hours. When the feature returned to 55°S, the rotation period decreased to 15.8 hours. Twenty-five days after the start of the cycle, the feature again drifted north with an associated increase of rotation period (*4*). The range of rotation periods spanned by D2 includes the 16.05 hour period of planetary radio emissions (*3*).

The latitudinal drift of the "Scooter" was small in amplitude (less than 2 degrees) and was neither monotonic nor periodic. The feature was initially detected at 42°S, where its rotation period was 16.74 hours; it remained at this latitude for more than three weeks. Then over the course of a week, the "Scooter" drifted north to 40°S, with a new rotation period of 16.76 hours. The "Scooter" then remained at this latitude for the remainder of the observations (Fig. 1A).

The Great Dark Spot drifted steadily northward at a rate of about 0.11° per day during most of the encounter period. During this time, its rotation period increased monotonically from 18.28 to 18.38 hours. For comparison, Jupiter's Great Red Spot displayed sinusoidal motion in longitude with a 90-day period and peak speeds between -1 and 5 m s^{-1} (*17*).

The Great Dark Spot exhibited a "rolling" motion around its circumference; the motion is anticyclonic and is best seen in time-lapse sequences (Fig. 4A). The boundary between the darker blue of the oval and the lighter blue outside the oval (Fig. 1A) changed shape as if a two-lobed structure were rotating inside it. Every 10 or 11 rotations of Neptune the long axis of the structure pointed east-west, and the GDS reached its maximum longitudinal extent. This configuration appeared twice during each rotation of the structure, whose fundamental period is therefore about 21 Neptune rotations (21 × 18.3 hours at the latitude of the GDS, or approximately 16 Earth days).

A rough estimate of vorticity within the GDS is 4π divided by the fundamental period, or 0.9×10^{-5} s^{-1}. In contrast, the vorticity of the ambient shear flow at the latitude of the GDS (assuming a difference in velocity of 100 m s^{-1} over 10° of latitude) is 2.3×10^{-5} s^{-1}. The vorticity of the GDS appears to be less than that of the ambient shear flow—the opposite situation from that of the Great Red Spot of Jupiter.

The interpretation of the rolling motion as wind (that is, fluid motion) is ambiguous. For example, it may represent the propagation of a wave around the edge of the Great Dark Spot. Associated with the rolling motion, the Great Dark Spot exhibited other morphological changes. For example, dur-

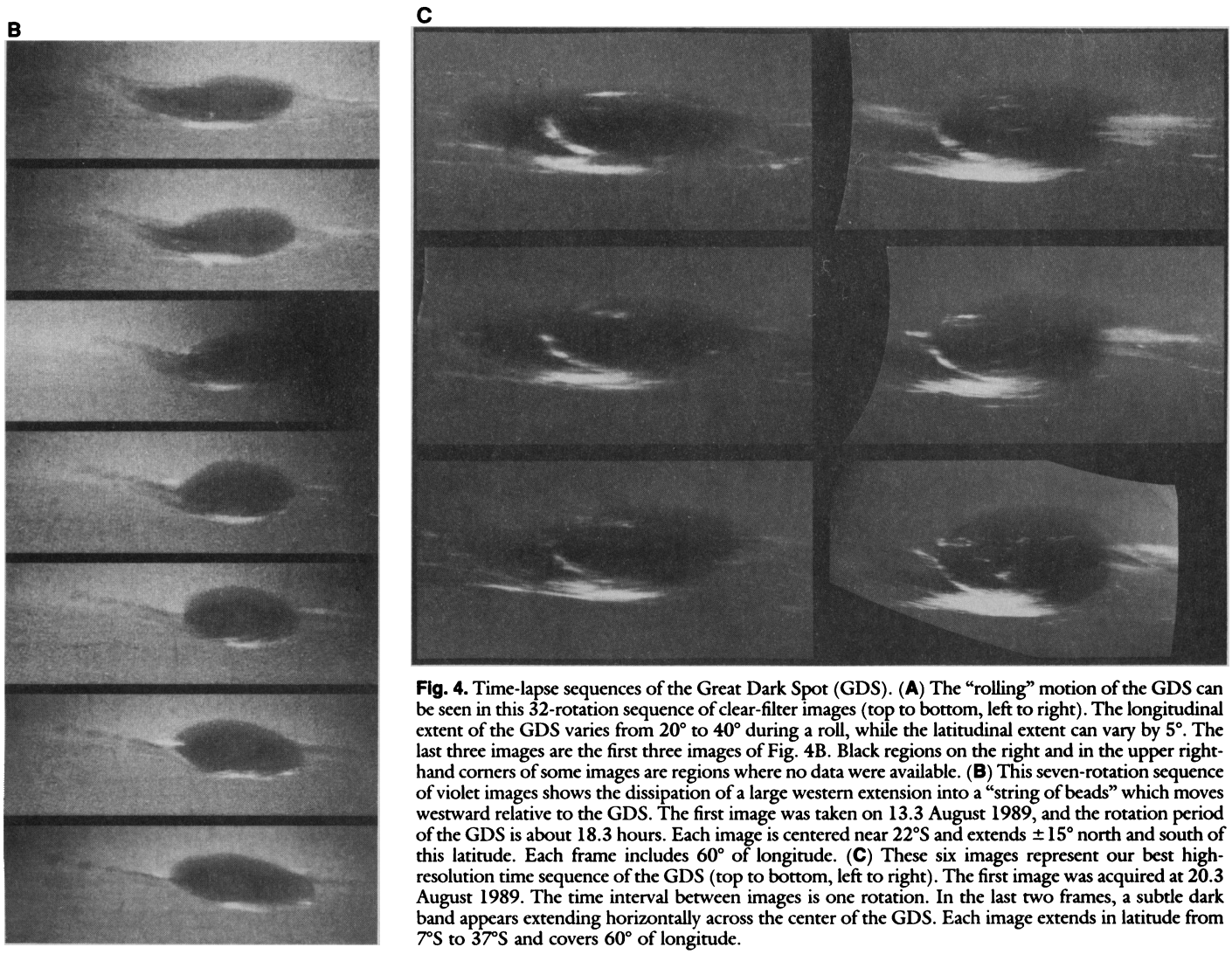

Fig. 4. Time-lapse sequences of the Great Dark Spot (GDS). (**A**) The "rolling" motion of the GDS can be seen in this 32-rotation sequence of clear-filter images (top to bottom, left to right). The longitudinal extent of the GDS varies from 20° to 40° during a roll, while the latitudinal extent can vary by 5°. The last three images are the first three images of Fig. 4B. Black regions on the right and in the upper right-hand corners of some images are regions where no data were available. (**B**) This seven-rotation sequence of violet images shows the dissipation of a large western extension into a "string of beads" which moves westward relative to the GDS. The first image was taken on 13.3 August 1989, and the rotation period of the GDS is about 18.3 hours. Each image is centered near 22°S and extends ±15° north and south of this latitude. Each frame includes 60° of longitude. (**C**) These six images represent our best high-resolution time sequence of the GDS (top to bottom, left to right). The first image was acquired at 20.3 August 1989. The time interval between images is one rotation. In the last two frames, a subtle dark band appears extending horizontally across the center of the GDS. Each image extends in latitude from 7°S to 37°S and covers 60° of longitude.

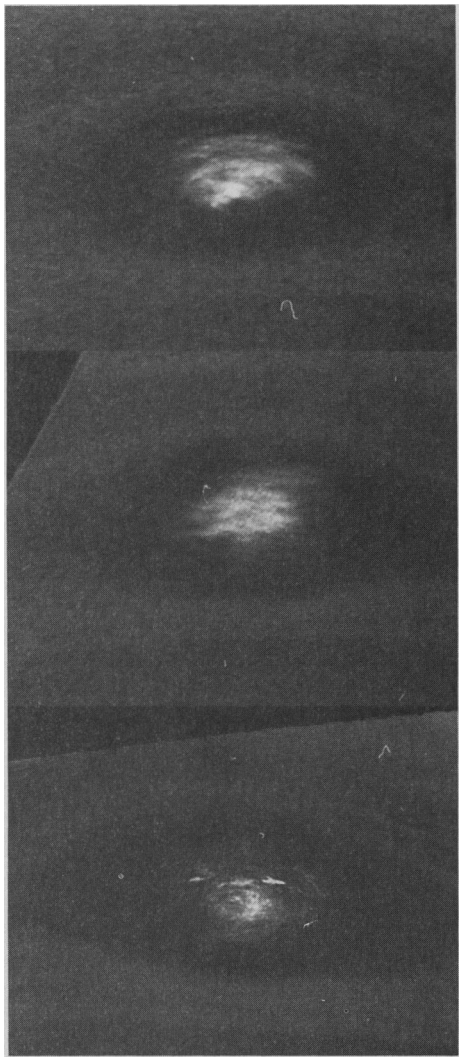

Fig. 5. Short-term variability in the core of D2. These three images of D2 are taken at intervals of one rotation (about 16 hours), beginning at 23.0 August 1989. They show the remarkably rapid growth and dissipation of detail in the core of D2.

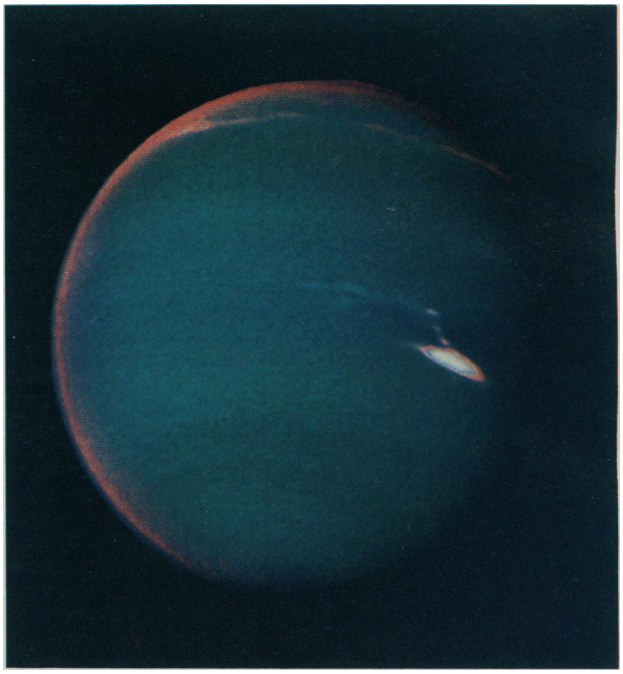

Fig. 6. False-color view of Neptune. This color-enhanced image was created with images taken on 22.7 August 1989 through the orange, MeU, and MeJ filters. The images were assigned to the blue, green, and red channels of the false-color image, respectively. High clouds appear red, while low clouds appear blue. The companion to the GDS is bright in all filters and is a high cloud, although its appearance here is distorted by saturation during image processing (as is the appearance of the northern cloud band near the western limb). The high-altitude haze layer shows up as a red region on the limb; the haze is transparent when viewed at normal incidence. Subtle shades of blue and green may represent differences in altitude, optical thickness, or composition of the cloud particles. [Image processing by L. K. Wynn]

ing one particular rotation, a series of dark cloud features (a "string of beads") developed after the maximum western extension of the Great Dark Spot occurred (Fig. 4, B and C).

Ground-based images have shown bright cloud features on Neptune for more than a decade (*18*). By comparing spacecraft images with near-simultaneous ground-based images, we identified the discrete bright feature seen this year in 890-nm ground-based images as the bright companion at 33°S associated with the southern edge of the Great Dark Spot (Fig. 8B). The GDS itself is not visible in the ground-based images. The bright features seen in previous years in ground-based images were located at 30°S in 1988 and 38°S in 1986 and 1987 (*18, 19*). Since the Great Dark Spot appears to drift in latitude by about 0.1° per day (*4*), it may have moved significantly over the last 3 years. If this is indeed the case, observers may have been detecting the Great Dark Spot companion as it drifted north and south, giving the Great Dark Spot a lifetime of more than 5 years. All ground-based images obtained prior to 1985 showed multiple bright features in both the northern and southern hemispheres (*18*).

The Great Dark Spot was not detected in ground-based images obtained at 550 nm, but a future search at 400 to 500 nm may have more success (see Fig. 10A). The Hubble Space Telescope should have sufficient resolution and wavelength coverage to detect the Great Dark Spot or any similar features. Other cloud systems that have been correlated with features in current ground-based images (*6*) are the south polar feature, the core of D2, some ephemeral bright streamers at the latitude of the Great Dark Spot and in the northern hemisphere, and the bright band surrounding the south pole (seen in MeJ images).

Zonal velocity profile. Hammel *et al.* (*4*) discussed the rotation period and zonal velocities of the four largest features visible in the Voyager images during the 80 days prior to encounter. Here we discuss the motions of smaller features observed during the last few days before closest approach. If the small-scale measurements and large-scale measurements were to disagree, we would suspect either that different altitudes were involved or that the patterns move relative to the wind, as with a propagating wave. At Jupiter and Saturn, the winds derived from tracking small features over short time intervals generally agree with those derived from the larger features when allowance is made for the tendency of larger features to move with the average flow in a latitude band. The measurement of velocity seemed to converge with smaller spatial and time scales. This

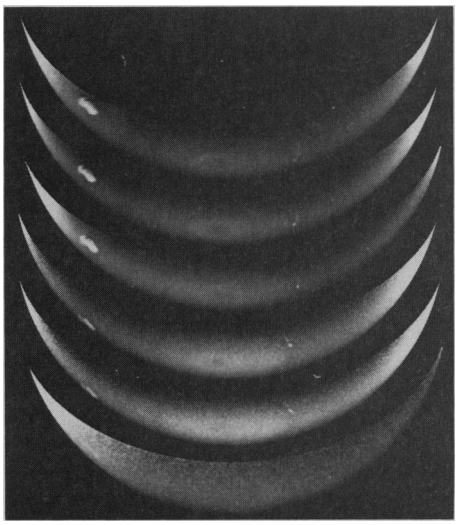

Fig. 7. Neptune's bright crescent taken in six filters (from bottom to top: UV, violet, blue, clear, green, orange) on 31.3 August 1989 (*7*). The images were shuttered in temporal order: violet, blue, UV, clear, green, orange. These images show the bright core of D2, the south polar feature, and the symmetric structure immediately surrounding the south pole. The relatively high contrast of the features in these images indicates that they extend above most of the scattering haze and absorbing methane gas in Neptune's atmosphere. [Image processing by D. A. Alexander]

agreement suggests that cloud displacements are indicators of the wind at roughly the same altitude for both of these planets.

On Neptune, the small-scale features evolve rapidly and disappear quickly, so the interpretation of cloud displacements is less straightforward (Fig. 4C). Because of the rapid evolution of small-scale features, the best measurement strategy must be a compromise. On the one hand, reducing the time interval over which displacements are measured reduces the effects of evolution of the features, and this ensures that they are recognized on successive time steps. On the other hand, the error in velocity goes up as the time interval is reduced. This error is proportional to the resolution in kilometers per line pair divided by the time interval (in other words, the speed of a feature that moves 2 pixels in one time step). By using sequences of three or more images, we can shift the focus from one rapidly evolving feature to another while broadening the time base. Although the error is reduced by this technique, there is still no guarantee that one is measuring actual fluid motion.

Not all regions on Neptune have small-scale features suitable for tracking. At scales of 50 to 200 km per line pair, there are eight general types of discernible cloud structures: (i) structure in the polar cloud feature at 71°S, (ii) variable brightening within the central region of D2 near 55°S, (iii) striations in the "Scooter" at 42°S, (iv) small bright features similar to the "Scooter" that appear in the latitudinal range from 40° to 50°S, (v) individual bright structures around the perimeter of the GDS, (vi) structure within the large-scale banding to the east of the GDS, (vii) details within the hazy bright equatorial patch located north of the GDS, and (viii) structure within the cloud bands at about 27°N.

Figure 13, A and B, gives the rotation periods and zonal velocities derived from both small-scale and large-scale features. Figure 13 reveals that measurements over different time intervals do not agree. The disagreement is particularly evident near 20°S and 70°S. The +'s and ×'s, for which the resolution per time step is less than 50 km per line pair, show less dispersion among themselves and better agreement with the solid curve. The diamonds, which use three or more images in a sequence, generally show less dispersion among themselves than the squares, which use image pairs only.

The measurements of the south polar feature (70°S in Fig. 13) provide an example of how the dispersion arises. The measurements fall into three groups. Those with rotational periods near 16.0 hours are derived from data with 49-hour time separation. Those with periods near 17.5 hours have 16-hour separation, and those with periods from 12 to 14 hours are from images separated by less than 2 hours. This grouping suggests that the observations in the first set track the large-scale structure measured during observatory phase (*4*), while the observations in the short-interval group track small-scale features that move through the larger structures.

Simple measurement error attributable to limited resolution is not the main source for the dispersion, particularly when three or more images are used in sequence. The dispersion is of order 300 m s^{-1}, whereas the error is only 50 m s^{-1} at 70°S (Fig. 13B). Wind shear with respect to altitude is one possible source. However, the infrared interferometer spectrometer (IRIS) observations of temperature as a function of latitude (*20*) suggest that the vertical wind shear is small, on the order of 30 m s^{-1} per scale height. For wind shear to be important, the structures must be distributed over a range of altitudes extending ten scale heights. The other possible source for the dispersion is propagation, either of the large-scale features or the small-scale features, relative to the fluid.

One interpretation is that the diamonds in

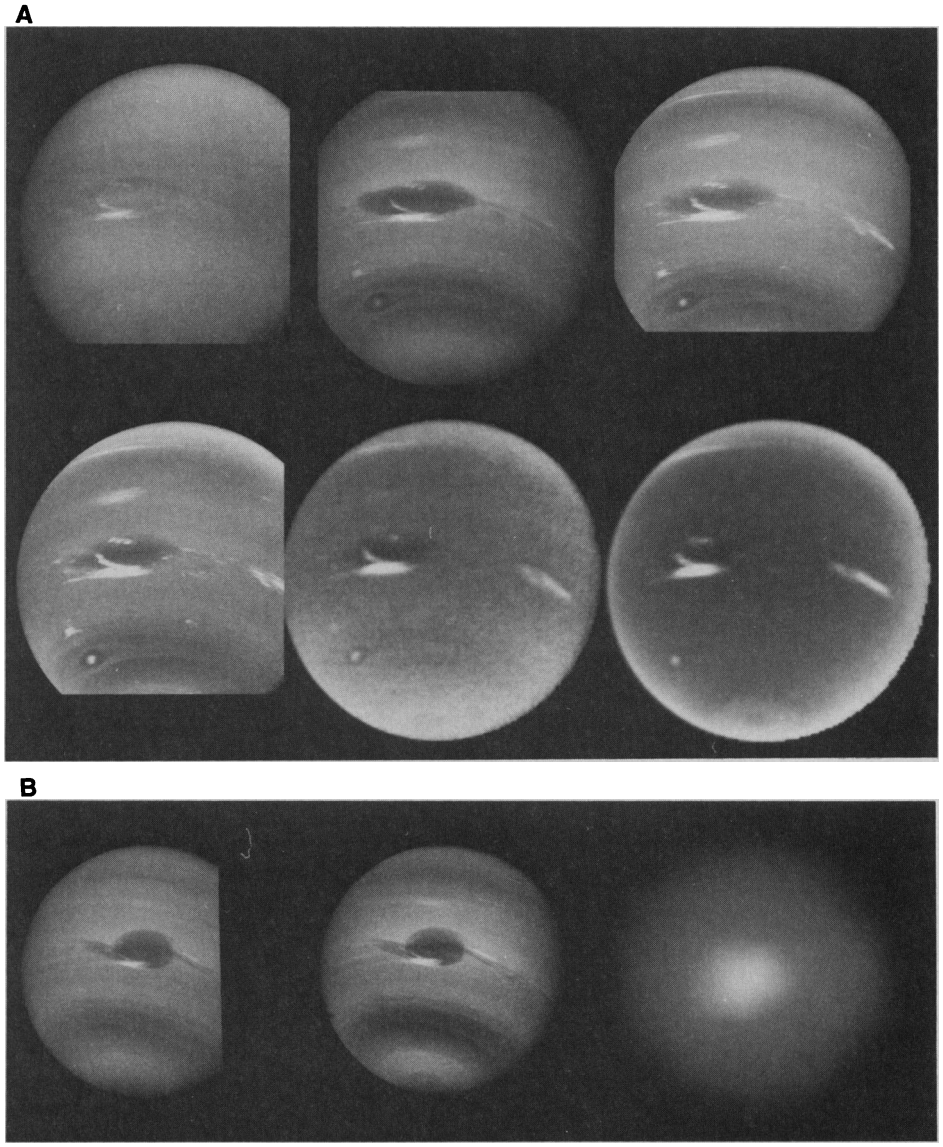

Fig. 8. Neptune's appearance as a function of wavelength (*7*). (**A**) Six images of Neptune taken in six Voyager filters (left to right, top to bottom: UV, clear, green, orange, MeU, and MeJ) on 21.3 August 1989. (**B**) These three images, obtained on 24.1 August 1989, show violet- and blue-filter images along with a near-simultaneous ground-based image taken in the strong methane band at 890 nm (the ground-based image was shuttered approximately 4 hours later than the spacecraft images to account for light travel time). Contrast of the Voyager images was increased by a constant amount (a factor of ~2.5). The ground-based image was stretched with a nonlinear function to enhance the cloud feature relative to the disk. Quantitative measurements of the relative brightnesses of specific regions are shown in Fig. 10A.

Fig. 13 represent the true motion of the fluid, making Neptune the windiest planet in the solar system. Wind speeds would then be close to the speed of sound, which is about 560 m s^{-1} at T-60K (Fig. 9). The solid curve might represent the slower motions at deeper levels or perhaps a large-scale wave. The other interpretation is that the diamonds and squares represent short-lived features that propagate relative to the flow. The solid curve, perhaps including the points at 5°N with periods near 19.5 hours and those at 27°N with periods near 17.5 hours, would then be our best estimate of the zonal wind. This is the most conservative interpretation, since the velocities of the large-scale features are the most certain.

Regardless of the interpretation of the points in Fig. 13, the periods of rotation at the equator are longer than both the radio period (*3*) and the periods at high latitudes. This fact puts Neptune in a class, with Uranus and Earth, of equatorial subrotators. Venus, Jupiter, Saturn, and the sun are all equatorial superrotators, since the periods of the equatorial atmospheres are shorter than those of the interiors. Neptune is by far the most extreme subrotator, as measured both by the speed of the atmosphere relative to the interior and by the fractional difference between the angular velocity of the interior and that of the equatorial atmosphere.

In general, subrotation at the equator is easier to understand than superrotation.

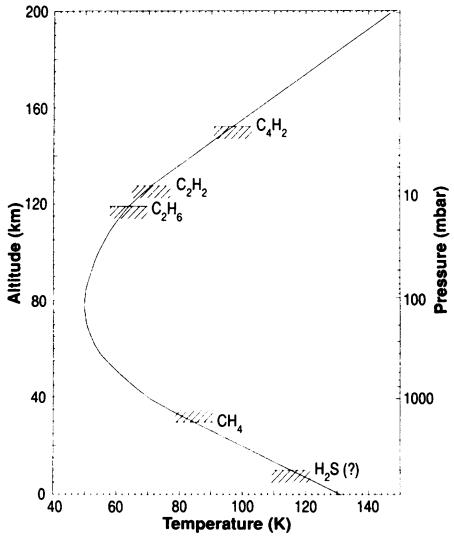

Fig. 9. Vertical aerosol structure of Neptune's atmosphere. The zero of altitude corresponds to the 4-bar pressure level. The existence of the main cloud deck near the 3-bar level was first inferred from ground-based spectroscopic observations of hydrogen quadrupole lines (*9*). The large tropospheric concentrations of methane gas derived from ground-based visible and infrared observations suggest the presence of a methane condensation cloud near the 1.2-bar level, but there is little direct observational evidence of a global methane cloud at this level. The bright cloud features seen in Voyager images may provide evidence for smaller-scale methane condensation clouds there. The existence of the high-altitude hydrocarbon aerosol layers was first predicted by theoretical models of Neptune's atmospheric chemistry (*13*). Brightness variations seen in limb scans of high-phase-angle Voyager images also suggest the presence of these aerosols.

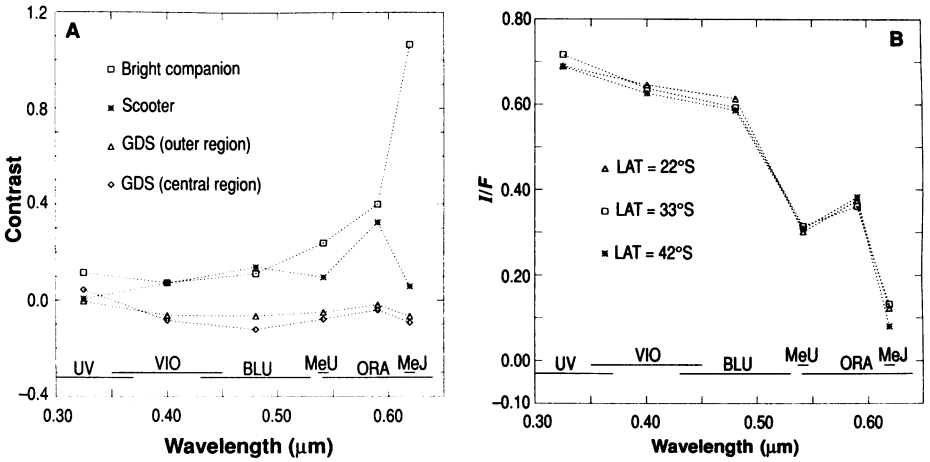

Fig. 10. (**A**) Contrast as a function of wavelength between discrete features and the nearby atmosphere. Contrast is defined as $(I_f/I_b - 1)$, where I_f and I_b are the brightnesses of a feature and its surrounding background, respectively. For the Great Dark Spot, two regions were measured, the central region and the outer edges. The contrast shown here for the bright companion was measured in low-resolution images. In higher resolution images, the feature was resolved into thin streaks (Fig. 3A), each of which has even higher contrast than that measured for the overall feature. The Voyager filter passbands are indicated along the bottom axis. (**B**) Reflectivity as a function of wavelength for the main cloud deck at different latitudes. The three curves show the wavelength-dependent absolute reflectivity (*I/F*) at latitudes 22°S, 33°S, and 42°S. The regions are at the same latitudes but different longitudes as the GDS, its bright companion, and the "Scooter," respectively. The feature contrasts shown in Fig. 10A were measured relative to these values. There are no significant differences between the measured reflectivities at these latitudes. Small differences in the reflectivity of other latitude regions give Neptune a banded appearance. The Voyager filter passbands are indicated along the bottom axis.

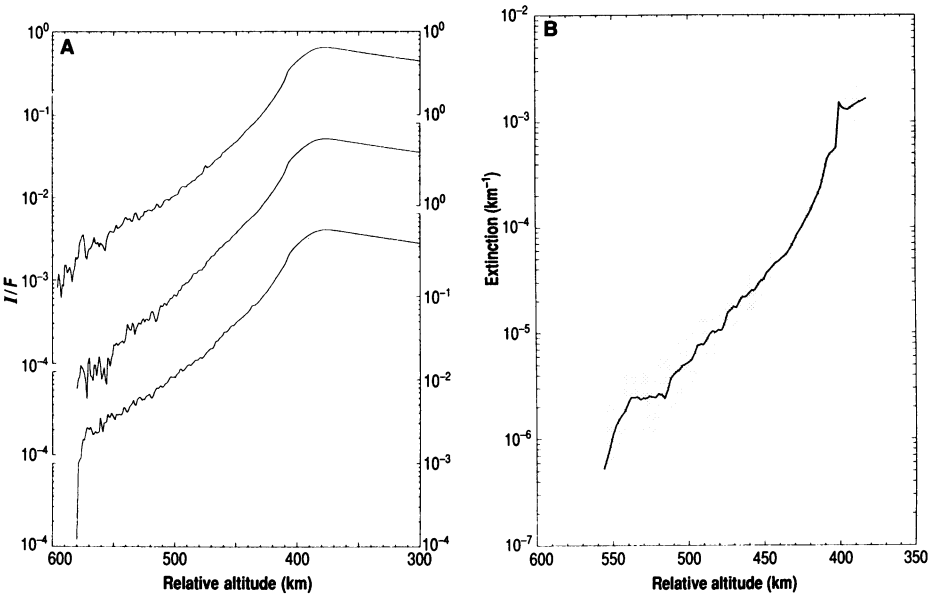

Fig. 11. Limb profiles of Neptune. (**A**) Radial scans across crescent images of Neptune's limb provide evidence for high-altitude stratospheric aerosol layers. These limb scans were extracted from a narrow-angle clear-filter image taken at a phase angle of 158°. The altitude resolution is approximately 1.9 km per line-pair. Image motion compensation prevented the spacecraft's translational motion from significantly smearing this image. The constant-brightness region extends from the main cloud top to a point near the tropopause (400 km on this plot; the zero of altitude is arbitrary). Brightness variations above this level indicate the presence of aerosols. (**B**) The steep slope of the vertical aerosol extinction profiles derived from the limb brightness scans in Fig. 11A indicates the presence of a discrete aerosol layer located almost 150 km above the tropopause (the stippled area encloses the uncertainty). This high-altitude aerosol layer may be related to the hydrocarbon condensation clouds predicted by theoretical models of Neptune's atmospheric chemistry (*13*).

Without dissipation, rings of fluid circling the planet at a given latitude tend to conserve their angular momentum as they move from one latitude to another. Maintaining equatorial subrotation merely requires taking rings of fluid from higher latitudes and moving them to the equator. Maintaining equatorial superrotation requires some pumping of angular momentum into the equator by organized waves or eddies.

The stability of a zonal flow depends not only on the velocity profile, but also on the density structure of the atmosphere. At the moment, we do not know the density field of Neptune's atmosphere over a sufficient range of depths and latitudes to do a comprehensive stability analysis. One necessary condition for stability, however, is that the angular momentum per unit mass, $\Omega r^2 \cos^2\varphi$, should decrease monotonically from equator to pole. Here Ω is the atmospheric angular velocity, r is the planetary radius, and φ is the latitude. On Neptune, as on Earth and Uranus, the decrease of $\cos^2\varphi$ outweighs the increase of Ω with latitude, and the condition is satisfied. This conclusion holds for all interpretations of Fig. 13 for which the equatorial period is less than 20 hours (*21*).

One of the most remarkable aspects of Neptune's zonal wind profile is its similarity to that found on Uranus (*1*). That these two planets, which have such different internal energy sources and such different obliquities, should have the same pattern of zonal winds requires an explanation that will certainly add to our understanding of atmospheric dynamics.

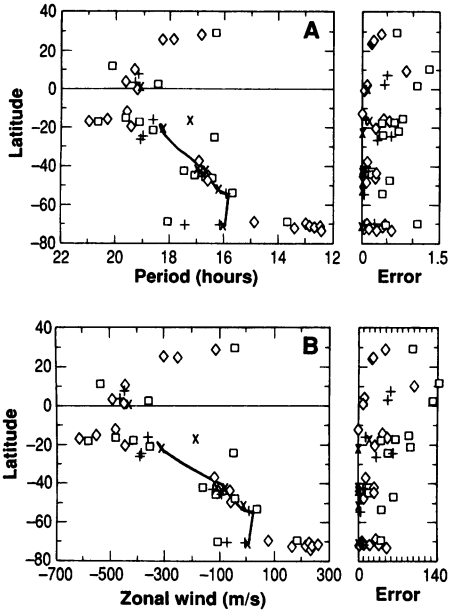

Fig. 13. Rotation periods (**A**) and zonal velocities (**B**) as a function of latitude. Velocity is measured with respect to the 16.1-hour period derived from the planetary radio emissions (*3*). The solid line represents the motion of the largest features over the longest time intervals (*4*). It is composed of nine individual measurements, two from ground-based observations and seven from the four largest features seen in the early Voyager images (3 of these were measured at two different latitudes). The symbols are measurements of individual small-scale features, often at time steps less than 2 hours and resolutions better than 100 km per line pair. The diamonds and crosses are values calculated with software developed at the University of Wisconsin in which displacements are measured in a sequence of three or more images. The squares and +'s use software developed at JPL in which displacements are measured in pairs of images only. The resolution (in km per line pair) divided by the time step (in hours) is less than 50 for the crosses and +'s and is greater than 50 for the diamonds and squares. The error estimates are in the same units as the figures and are computed from the statistics of the observations.

The Neptune Ring System

Prior to the Voyager reconnaissance of Neptune, very little was known of its ring system. By August 1989, about 50 stellar occultations had been observed from ground-based observatories, representing 100 separate scans through the system. Although more than 90% of these observations yielded no detection, at least five occultations observed between 1981 and 1985 demonstrated with high confidence the presence of material in orbit around Neptune (*22*).

One of these observations was a detection, observed by more than one telescope, of either a small satellite or an optically thick, azimuthally incomplete ring of about 80 km radial width. Several other detections, two of which were confirmed, indicated narrower (approximately 15 to 25 km) but also discontinuous rings. Minimum inferred lengths were 100 km. Thus, the existence of relatively narrow "ring arcs" orbiting between 41,000 and 67,000 km from Neptune was commonly accepted.

On the basis of these ground-based observations alone, however, it was impossible to distinguish between a family of permanent or transient arcs around Neptune or continuous rings of highly variable optical depth. Neptune's ring features became members of a sparsely populated class of ring structures including the narrow, azimuthally incomplete rings in Saturn's ring system [in the Encke gap, the Cassini Division, and around the F ring; see, for example, (*23*)] and possibly in the Uranian ring system as well (*24*).

The presence of short evolutionary timescales in ring systems is a well known and as-yet unsolved puzzle (*25*). The time required for longitudinally localized material 20 km in radial width to spread 360° as a result of differential rotation is only about 5 years. Stable, non-transient ring arcs would obviously require a longitudinal confinement mechanism (*26, 27*); transient arcs require the continual creation, dispersal, and replenishment of local concentrations of ring material. We present here the initial results on the nature and dynamics of Neptune's rings from analyses of Voyager imaging observations, discuss the various theories suggested for the existence of arcs in light of our findings, and compare Neptune's system

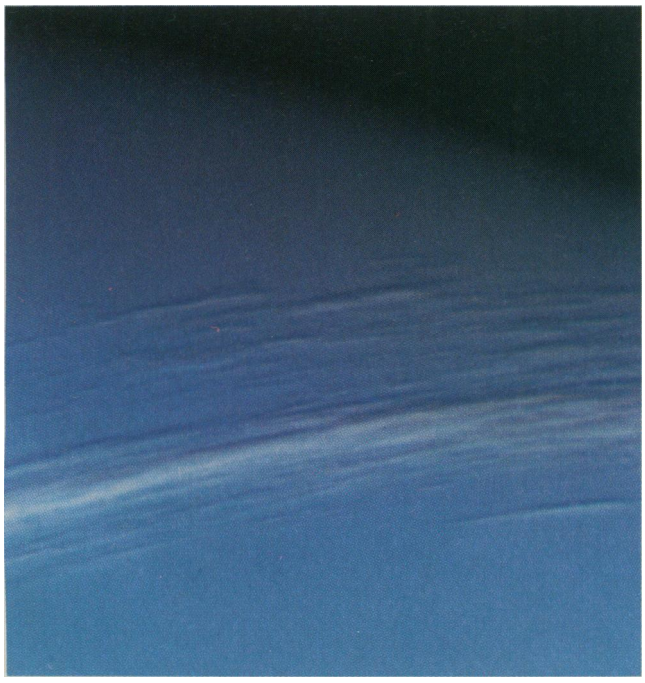

Fig. 12. Cloud shadows in the northern hemisphere. Bright cloud bands near the terminator at latitude 27°N appear to cast shadows on the main cloud deck. Measurements of these shadows indicate that the tops of these cloud bands are 100 ± 50 km above the background cloud deck. Similar shadows were seen for clouds in the south polar region. This image was created by combining violet-, green-, and orange-filter images acquired near closest approach at 25.1 August 1989. [Image processing by G. W. Garneau]

with the other ring systems we see in the outer solar system.

Radial distribution of ring material. The Neptune ring system, as seen in Voyager images, contains two narrow rings, 1989N1R and 1989N2R, at radial distances of 62,900 km and 53,200 km, respectively; a broad ring, 1989N3R, at a radial distance of 41,900 km; a second broad ring, 1989N4R, extending outwards from 1989N2R to a distance of nearly 59,000 km; and an extended sheet of material that may fill the inner Neptunian system. (We will alternatively refer to 1989N1R, 1989N2R, and 1989N3R as the N63, N53, and N42 rings.) The N63 ring is outermost and includes three arcs of substantially greater optical depth than the ring average. The three arcs are clustered together within a total range of 33 degrees in longitude. 1989N1R and 1989N2R lie about 1000 km outside the newly discovered satellites 1989N3 and 1989N4, respectively.

Neptune's rings were most easily visible at the moderately high phase angles obtained after closest approach to the planet, and three images at these phase angles best characterize the overall distribution of material. Figure 14, a 111-second exposure, and Fig. 15, a composite of two 591-second exposures taken 1.5 hours apart, were all imaged through the clear filter of the wide angle camera and show the ring system at forward scattering phase angles of about 135°. Figure 14 clearly shows the arcs which are 12 data number units (DN, out of a total range of 255 DN) above background. In comparison, Fig. 16 is also a 111-second exposure taken through the clear filter of the Voyager wide angle camera, but at a phase angle of only 15.5°. It shows the same three arcs within the optically thin N63 ring; the second, even fainter N53 ring is also visible. Though Fig. 16 is one of the best Voyager images taken of Neptune's ring system at low phase, the average brightness in the arcs measured only about 2.5 DN above background.

The arcs were not captured in Fig. 15 because of the 50 degrees of orbital motion between the two frames. However, one can easily see the N63 and N53 rings as well as

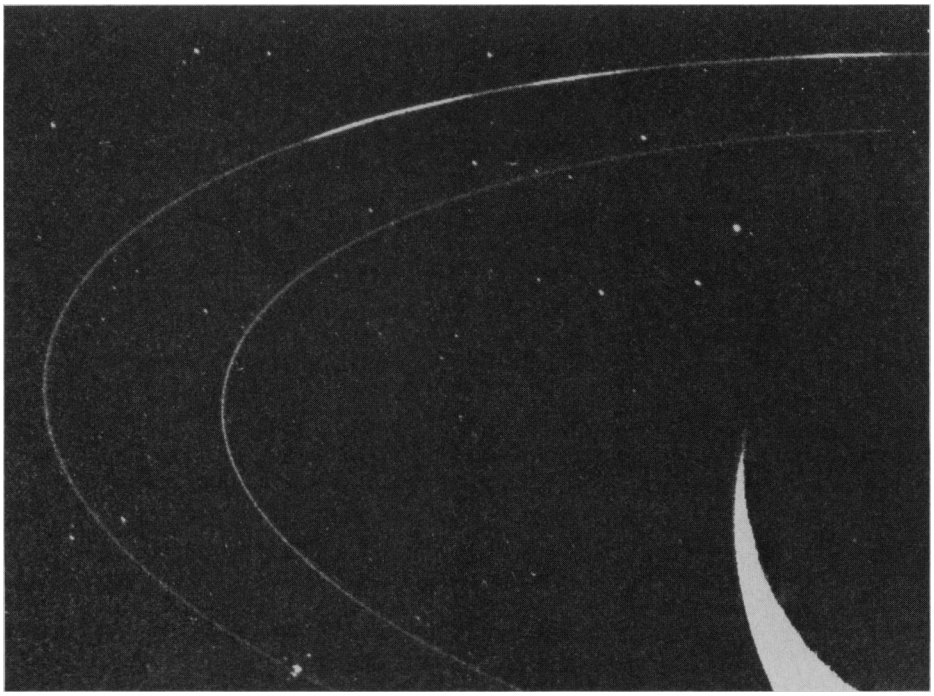

Fig. 14. This Voyager 2 image (FDS 11412.51), a 111-s exposure obtained through the clear filter of the wide angle camera, shows the ring system in forward scattering geometry (phase angle of 134°). Clearly seen are the three ring arcs and the N53 and N63 rings. The direction of motion is clockwise; the longest arc is trailing. The resolution in this image is about 160 km per line pair; the trailing arc was imaged at this same time at a higher resolution of about 20 km per line pair (Fig. 18).

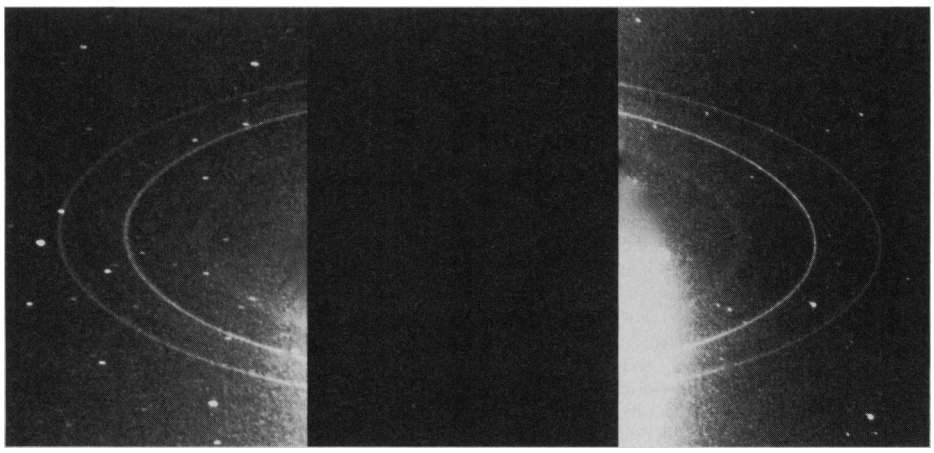

Fig. 15. This pair of Voyager 2 images (FDS 11446.21 and 11448.10), two 591-s exposures obtained through the clear filter of the wide angle camera, shows the full ring system with the highest sensitivity. The ring arcs seen in Fig. 14, however, were at an unfortunate orbit longitude and were not captured in either of these frames taken 1.5 hours apart. Visible in this figure are the bright, narrow N53 and N63 rings, the diffuse N42 ring, and (faintly) the plateau outside of the N53 ring (with its slight brightening near 57,500 km). [Image processing by L. A. Wainio].

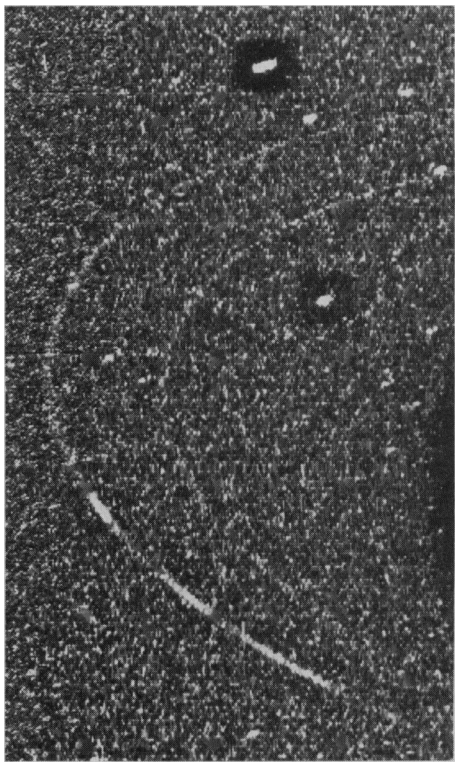

Fig. 16. This Voyager 2 image (FDS 11350.23), a 111-s exposure obtained through the clear filter of the wide angle camera, shows the N53 and N63 rings faintly in backscattered light (phase angle of 15.5°). Relatively prominent in the N63 ring are the three Neptune ring arcs. The satellite 1989N2 can be seen in the upper right corner, streaked by its orbital motion; the other bright object is a star. The arcs are unresolved in this image (resolution of 37 km per line pair); their apparent width is due to image smear.

N42 (1989N3R). This latter ring, which is seen at low phase angles only with great difficulty, is clearly resolved and has a full width at half maximum of about 1700 km. Also faintly visible in Fig. 15 is a sheet of material beginning midway between the two outer rings at approximately 59,000 km and possibly extending down to the planet. (We discuss this further below.) There are identifiable features within this sheet. The most prominent among them is the plateau, 1989N4R. A distinct feature or ring at 57,500 km, 1989N5R, on the outer edge of the plateau, can be seen above and below the ansa in Fig. 15. In addition, there are hints of other radial structure in the plateau.

Although one gets the impression from Fig. 15 that material extends continuously inward from 59,000 km, this is difficult to confirm because of the uncertainty in the distribution of scattered light. Figure 17 is a radial profile of the intensity seen in the left hand frame of Fig. 15. In this scan, a smooth function has been subtracted to remove the scattered light from the planet; this has the effect of tapering off the brightness distribution to zero at small radii. Though this removal of scattered light is uncertain, the N42 ring does appear to be embedded in material which extends out to the N53 ring, with brightness only slightly less than that of the plateau region but having a local minimum at 52,000 km, approximately the orbit of 1989N3. A similar configuration was observed in the Uranian system between Cordelia and the λ ring (1986U1R) (*1*).

In other high-phase frames, a narrow, clumpy ring (as yet unnamed) is also visible just interior to 1989N1R. This feature is not seen in any low phase angle images, and appears to lie at about the same radius as satellite 1989N4. Imaging observations of the arcs and the satellites within the ring region indicate beyond doubt that the direction of orbital motion is prograde. Because of remaining uncertainties in the Laplacian plane pole orientation, we cannot at the present time completely rule out very small ring eccentricities and inclinations relative to this plane, which presumably is identical to that of the inner, regular satellites.

Voyager observations have put strong constraints on the existence of a potential polar ring system (*28*); several high and low phase angle images of Neptune's north and south polar regions, covering a radial range out to several hundred thousand kilometers from the planet, reveal nothing. Although the upper limiting optical depth for broad sheets of material is roughly 10^{-5}, it is still impossible to rule out the existence of narrow clumps in polar orbits with somewhat higher optical depths.

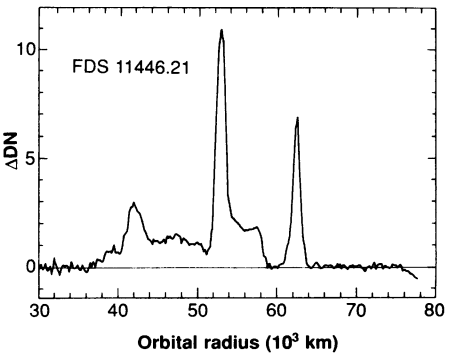

Fig. 17. This radial profile of the brightness of the rings as seen in Fig. 15, in units of DN (data number) above background as a function of orbital radius, was obtained by averaging all points lying within narrow radial bins and excluding the stars. A smooth background has been subtracted out to account for glare from the planet; since the true background is uncertain, it is not possible to say whether the rings extend all the way in to the planet.

High-resolution imaging coverage of the rings, excluding the arc retargeting that is discussed below, was made mostly at sky plane resolutions of 15 and 40 km per line pair. Due to the smear resulting from the long exposures, we have been unable to resolve in the radial direction either the N53 ring or the non-arc part of the N63 ring. Our highest resolution images, obtained within 13 hours of closest approach, were of the arcs and were retargeted approximately 4 days before closest approach, based on earlier imaging observations of arc locations and orbital motion.

The single highest resolution frame, FDS 11386.17, has a sky plane resolution of only 3.0 km per line pair. At the geometry of this observation, radial foreshortening results in a ring-plane resolution of 15 km per line pair. The trailing arc has a full radial width at half maximum that is close to the resolution of the camera. However, in our narrow angle outbound retargetable image (Fig. 18), measurements of variations in the ring width indicate that the ring may be just barely resolved, implying a radial width of about 15 km. This value is in good agreement with the groundbased and Voyager photopolarimetry stellar occultation measurements (*22, 29*).

Longitudinal distribution of material. On longitudinal scales of a radian, all three rings and the plateau region are continuous around the planet. This is very clearly seen in forward-scattering geometry (Fig. 15), but it is also evident, though with greater difficulty, in backscattered light for the N53 and N63 rings. On intermediate scales, the only prominent structures are the three bright arcs seen in the N63 ring (Figs. 14 and 16). The azimuthal lengths of these arcs, measured to be the distance between the half-

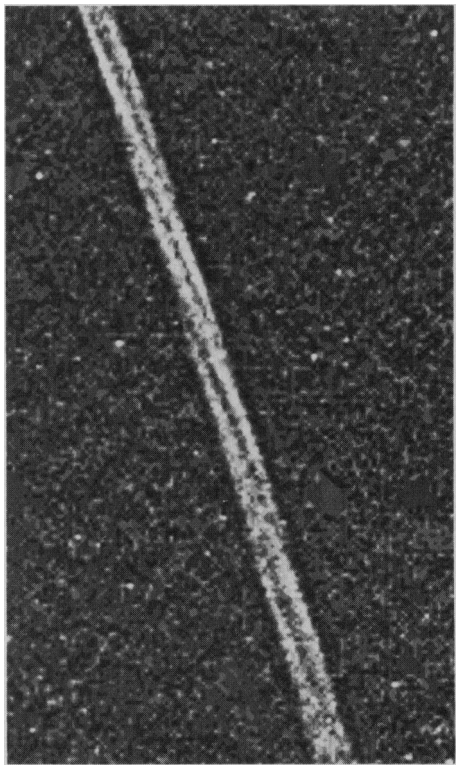

Fig. 18. This narrow angle, clear filter image (FDS 11412.46) was part of the outbound (high phase angle) retargetable sequence along with Fig. 14 and shows a portion of the trailing arc. The sky plane resolution is about 14 km per line pair and the phase angle is about 135°. The combination of uncompensated spacecraft motion and ring orbital motion causes points to streak in the image. However, the width and separation of the streaks reveal the scale size and longitudinal distribution of clumps in the rings. In addition to the fine scale information revealed in the streaked clumps, this image seems to show width variations which would imply that the arc may be resolved (see text).

intensity points in azimuthal brightness scans in Fig. 14, are approximately 4°, 4°, and 10° for the leading, middle, and trailing arcs, respectively. The distances between the midpoints of these features are about 14° (leading-middle) and 12° (middle-trailing). To within the measurement uncertainties, the same values are obtained from low phase images. Given the signal-to-noise ratio of the data, we find no convincing evidence at this time for longitudinal structure on scales greater than about 5° in either of the two remaining rings or in the remainder of the outer ring in either forward or backscattering geometry.

Small-scale azimuthal structure is most easily seen in the retargeted image of the trailing arc taken at high phase (Fig. 18). Several long linear features are apparent, which we believe are formed by discrete clumps in the ring, trailed out by a combination of orbital motion along the ring and the motion of the spacecraft across the ring.

These features are unresolved and appear to be associated with microscopic particles because of their enhanced brightness in forward scattered light (phase angle of 135 degrees). One of the retargeted images taken of the trailing arc at low phase shows structure similar to that seen in Fig. 18 when the image contrast is strongly enhanced. Though it is not yet certain if these are the same clumps seen in Fig. 18, it is noteworthy that the typical separation between these clumps, approximately 0.1° to 0.2°, is the same in both frames. A similar object within the leading arc is seen in another low phase image not reproduced here. These features may be large embedded ring particles or associated clumps of debris similar in morphology to the discrete features found in the F-Ring or Encke gap ringlet of Saturn (*23*).

Moonlet search. A search for additional small satellites orbiting near the rings of Neptune is still being conducted (*30*), but the lack of confirmed sightings implies that few or no additional satellites larger than 12 km in diameter with assumed geometric albedo of 0.05 are orbiting in the ring region. To discriminate actual sightings from noise, we required each candidate object to be in a circular, equatorial orbit. Because of this requirement, our limiting radii are roughly twice as large for satellites with orbits inclined by more than 10° or eccentric by more than 0.1.

Ring photometry and particle properties. The ability of spacecraft to observe a system over a range of viewing angles is of great importance to our understanding of planetary ring systems, since the scattering behavior of particles of microscopic and macroscopic sizes differs dramatically with phase angle. Observations at high phase angles (>150°) have been important in establishing that the microscopic "dust" particle fractional area in the main rings of Saturn and Uranus is quite small—between 0.01 and 0.001 by area (*31*). In other rings, the dust fraction can be considerably larger; for example, Saturn's F ring, a narrow, clumpy ring, and Saturn's E ring, a broad, diffuse ring, are both visible primarily because of microscopic particles—dust fractions greater than 80% (*32*). In the case of Neptune, the spacecraft trajectory did not allow any extremely high phase-angle observations; however, the rings themselves compensated for this lack of observational sensitivity by being extremely "dusty."

Our preliminary photometric analysis relies on only two phase angles (approximately 14° and 135°) for the following regions: the middle arc of 1989N1R, wide azimuthal averages in the N42, N53, and N63 rings (excluding the arc material) and the constant brightness region ranging between 54,500 and 57,500 km from Neptune. In order to suppress the effects of possibly variable smear in the long exposures that were used, the radial integral of the brightness profile, or "equivalent width," was employed (*33*).

Figure 19 shows the observations for the different regions, converted to the quantity $\omega_0 P \int \tau dr$, as functions of phase angle (*33*). The fact that all regions are more reflective at high phase angles is direct evidence for a substantial dust population, since the brightness of macroscopic objects depends primarily on the fraction of the visible illuminated area and decreases by an order of magnitude as phase angle increases over this range. We have modeled the particle properties in these regions to obtain the optical depth of macroscopic and microscopic material, using assumptions as to the individual particle properties based on prior experience. We have assumed that the large macroscopic particles in the Neptune ring system have the Uranus ring particle phase function and a Bond albedo between 0.01 and 0.02, which brackets the Uranus ring particles, Phobos, Diemos, and Amalthea. This combination results in a geometric albedo of about $p = 0.05$, similar to that seen for the newly discovered Neptune satellites.

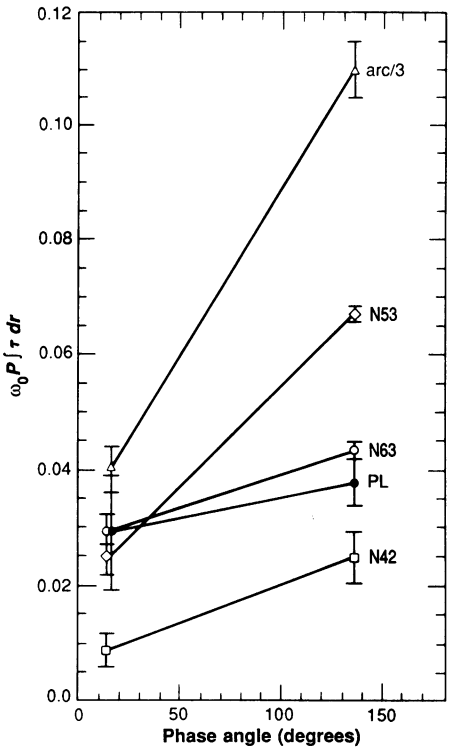

Fig. 19. In this figure, observations of the radially integrated brightness of different regions of the Neptunian rings are shown as functions of phase angle. The brightness has been converted to the "equivalent width" product $\omega_0 P \int \tau dr$, in units of kilometers, where $\int \tau dr$ is the "equivalent depth" and τ is the normal optical depth. The regions are the N42, N53, and N63 rings (not including the ring arcs), the plateau region averaged between 55,000 and 58,000 km, and the middle ring arc (plotted at one-third of its actual values).

To bound the properties of the microscopic dust component, we chose coal dust (which is used to model the Uranus rings) and a typical silicate (which is used to model the Jupiter ring). Mie scattering, as modified by a simple irregular particle algorithm, was used to obtain the range of dust particle albedo and phase functions for material with this range of composition. We assumed a power law size distribution with index of 2.5, such as has been observed to characterize the dust in the Uranus and Jupiter rings; microscopic dust in ring systems tends to have a somewhat flatter size distribution than typical comminution products due to the size dependence of removal processes. The results of this preliminary photometric modeling are shown in Fig. 20.

The N42 ring and the plateau are clearly low optical depth structures, although two orders of magnitude more substantial than the Jupiter ring or the E and G rings of Saturn and about one order of magnitude more substantial than the Uranus dust bands. The optical depth of the middle arc, about 0.04 to 0.09, is in excellent agreement with ground-based values when appropriate diffraction corrections are made. Within the uncertainties, the N42, N53, and arc regions have the same dust fraction (0.5 to 0.7), which is about twice as large as the fraction found in the N63 ring and the plateau regions, and significantly larger than found in the main rings of Saturn or Uranus (10^{-3} to 10^{-2}).

Comparison of ground-based and Voyager observations. Re-analysis of the geometries for the most reliable ground-based stellar occultation tracks by means of the improved Voyager Neptune pole position has indicated that the observations of 22 July 1984, 7 June 1985, and 20 August 1985 are all consistent with occultation by material near the radius of 1989N1R (*34*). These are also the only three observations which yield equivalent widths of up to 2.0 km, consistent with the abundance of material that we find in the three Voyager arcs (Figs. 19, 20) when diffraction effects are appropriately accounted for. Although this suggests that the Voyager arcs are the same as those observed from Earth in 1984 and 1985, a much more stringent test of this hypothesis, and one that could rule out the notion of transient and evolving arcs, would be the successful prediction of longitudinal location at the time of the Voyager encounter by use of the observed arc locations in both ground-based and Voyager observations and the mean motion derived from Voyager images.

A precise determination of the arcs' mean motions must necessarily await careful arc position measurements in images spanning as large a temporal range as possible, and the fitting of such measurements with a general model describing an eccentric and inclined orbit, as well as an evaluation of the pole of Neptune's Laplacian plane, which is independent of the assumed ring arc model. A preliminary value was obtained, however, by assuming the arcs' orbits to be identical, circular, and equatorial [Neptune rotational pole orientation, (α, δ)1950 = (298.904, +42.841)], and by measuring the beginning and ending longitudes of each arc in smoothed, radially averaged, azimuthal scans taken from at most five images spanning a total of about 6.5 days. For each of the three arcs, a weighted least-squares fit to the measured locations versus time was used to determine the mean motions; the final value and its uncertainty, 820.12 ± 0.06, are the mean and the standard error of the mean, respectively, of these three numbers. Using this value, we projected forward from the longitudes of arc detection in the three reliable ground-based stellar occultations in the N63 region mentioned above (*35*), correcting for light travel time, to the epoch of our best single image (FDS 11412.51, Fig. 14): for 22 July 1984, the precessed longitude is 227°; for 7 June 1985, 238°; and for 20 August 1985, 224°. The large uncertainty in the rate, 0.06° per day, maps into a longitude uncertainty at the time of Fig. 14 of approximately ±100°. Nonetheless, the agreement found with the use of the nominal rate is astonishingly good: the ground-based observations fall within about 15° of each other and comfortably intercept the longitude range, 206° to 240°, subtended by the three arcs in Fig. 14. (Although the ground-based longitudes are measured in the Neptune-Triton invariable plane, and the Voyager longitudes in the Neptune equator plane, the difference amounts to at most a few degrees.)

We consider these results convincing evidence that the Voyager arcs themselves were the occulting material for all ground-based occultations at this radius and, therefore, that the arcs are stable over intervals of at least 5 years. Future work in this area, taking into account the geometrical considerations mentioned above, may in fact allow us to determine with high probability which of the three arcs was observed in each of these three ground-based occultations and to predict the locations of these features at the times of upcoming Neptune stellar occultations observable from the ground or from the Hubble Space Telescope. It is not surprising that ground-based observations, in general, do not detect material in the non-

Fig. 20. In this figure, we have estimated the total optical depth and fraction in microscopic dust particles from the data of Fig. 19, making certain assumptions as to the phase function and albedo of the ring particles. The total normal optical depth, plotted vertically, has been obtained from the equivalent depth by dividing by a physical width of 15 km for N53, N63 and the arc, by the 1700-km full-width at half maximum for N42, and by the 3000-km width of the plateau. The fraction of this total represented by "dust" is plotted horizontally. In all cases, the patches are bounded on the lower right and upper left by large particle single scattering albedos of 0.02 and 0.01 respectively, and on the upper right and lower left by microscopic material composed of coal and of silicates, respectively. The large particle phase function and the dust particle size distribution are those of the Uranus ring particles. Although these specific values are clearly model-dependent, the relative differences between the regions (that is, corresponding corners of the patches) are real.

arc regions of the N53 and N63 rings—the estimated optical depth of 0.01 to 0.02 in these regions is below the ground-based threshold. However, it is worth noting that (unconfirmed) ground-based stellar occultation observations, revised by using Voyager improvements for the Neptune pole orientation (*35*), indicate events at around 42,000 kilometers and 55,000 kilometers—opening the possibility that clumpy material may now, or did then, exist in regions where we now observe broad, diffuse belts of material (see Fig. 21).

One other important result concerns the identity of the object that was responsible for the first occultation observation of material orbiting Neptune (*22*). Using the mean motions for the small satellites determined from imaging observations, we obtained their positions at the time of the 1981 event. Since this event did not occult the planet, some astrometric uncertainty remains in addition to the uncertainty in the mean motion of the candidate satellites. However, we find that 1989N2 falls within the total uncertainty (about 8° of orbital longitude or less than 1 arc second) of the location of the event, and that the only other possible candidate (1989N4) is on the other side of the planet. This excellent positional agreement, combined with the fact that the 1981N1 occultation was completely opaque and 180 km across and 1989N2 has a diameter of about 200 km, makes us confident that 1981N1 and 1989N2 are one and the same object (Fig. 21).

Discussion of ring observations. Despite the singular nature of Neptune's system of relatively large satellites (in particular, retrograde Triton and highly eccentric Nereid), and despite the dramatically different visual impression that Neptune's rings give in comparison with those of Jupiter, Saturn,

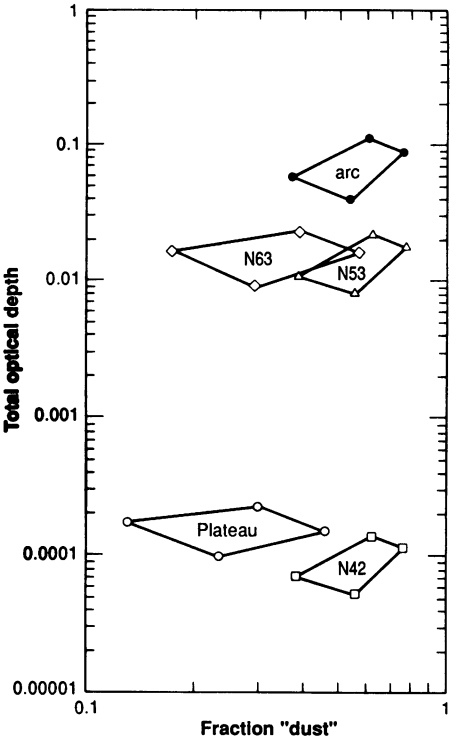

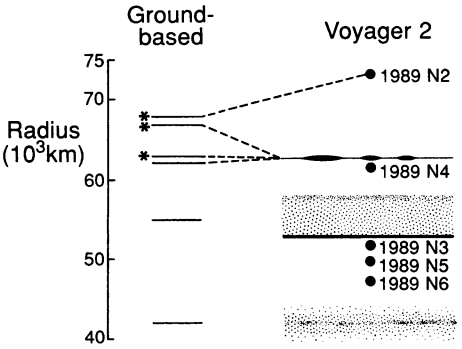

Fig. 21. This figure shows the radial locations of the most reliable ground-based occultation detections of material around Neptune compared against the locations of ring material as seen in Voyager imaging data. Asterisks denote ground-based observations confirmed by more than one telescope.

and Uranus, the combined system of rings and inner satellites has surprised us by sharing many characteristics with the other giant planet ring-satellite systems. To wit, Neptune's rings comprise an extensive prograde system, essentially confined to the planet's equatorial plane and filling the planet's Roche zone, a region lying between the classical stability limit for a liquid satellite [$r/R_p = 2.44\ (\rho_s/\rho_p)^{0.33}$, where ρ_s and ρ_p are the densities of the satellite and the planet, respectively, R_p is the planet's radius and r is the distance from the planet's center] and the "accretion limit" at which equal-sized particles are destabilized by differential Keplerian motion [$1.44\ (\rho_s/\rho_p{}^{0.33})$] (*36*).

It is a system containing narrow dusty

Table 1. Small satellites of Neptune, where a is the semimajor axis.

Satellite	a (10^{+3} km)	Mean radius (km)	Geometric albedo	Best resolution (km per pixel)
Nereid	551	170 ± 25	0.14 ± 0.035	43.3
1989N1	117.6	200 ± 10	0.060 ± 0.006	1.3
1989N2	73.6	95 ± 10	0.056 ± 0.012	4.1
1989N3	52.5	75 ± 15	0.054 ± 0.024	16.9
1989N4	62.0	90 ± 10*		18.4
1989N5	50.0	40 ± 8*		17.4
1989N6	48.0	27 ± 8*		23.6

*Assumes albedo equivalent to 1989N1 and 1989N2.

rings, like the Uranus λ ring (1986U1R) and the Saturn F ring; diffuse dusty rings, perhaps similar to the Jupiter ring and Saturn G ring; azimuthally confined arcs embedded with a ring, reminiscent of Saturn's F and Encke rings; and possibly a broad sheet of dust like that which is seen around Uranus at high phase angles.

An examination of Neptune's system of satellites and its distribution with orbital radius (Table 1) supports the generality that, as the distance from a giant planet decreases, there is a gradual transition from large, isolated satellites to families of more numerous, smaller satellites and ring material. The presence of relatively massive objects (for instance, satellites at Neptune, rings at Saturn) well within the outer planets' Roche limits, where structural stability depends on internal strength but where accretion to radii of tens of kilometers is difficult or impossible, supports the idea that the parent objects of these outer planet ring-satellite systems migrated into their respective Roche zones from elsewhere long ago (*37*).

In comparing only Uranus with Neptune, we find that the reflectivities of the surfaces of their inner satellites are similar and very low. Also, the agreement between our derived Neptune ring arc optical depths and those obtained from ground-based stellar occultation measurements supports equivalently low albedos for the ring particles, comparable to those found for Uranus. Compositionally, therefore, the Neptune and Uranus ring-satellite systems appear to be quite similar, suggesting chemical origins and/or evolutionary histories that proceeded in tandem, histories that may well characterize the outer solar system beyond Saturn.

However, the dramatic differences also call for our attention. The amount of mass in Neptune's rings is approximately 10,000 times less than that at Uranus and many orders of magnitude less than that at Saturn, yet the inner Neptune satellites are significantly larger, and presumably more massive, than the bodies in similar locations in the ring-satellite systems of the other giant planets. At Neptune, the five satellites 1989N2 through 1989N6, with diameters ranging from approximately 55 to 190 km, all fall within the Roche "liquid" limit at roughly 77,000 km; at Uranus, the nine satellites falling within its Roche limit, 1986U1 through 1986U9, range from about 25 to 110 km in diameter (*38*). If we assume the overall satellite-size distributions to be similar among the outer planets, the relatively large number of big bodies close to Neptune might lead one to expect a proportionately large abundance of smaller moonlets in the ring region. Yet, our search for satellites to date does not support the existence of more than two objects (1989N5 and 1989N6) with diameters less than 100 km.

Evidently, the distribution of mass among the inner satellites of each planet, and between each planet's satellites and rings, is very different. The absolute amount of mass within these zones is also notably different: All the mass in Saturn's rings, which fill Saturn's Roche zone, can be contained within an icy body approximately the size of Mimas, 195 km in radius; in Neptune's Roche zone, the rings' and satellites' masses can be contained within an icy body 130 km in radius; and for Uranus, within an icy body 75 km in radius. It is interesting to compare these differences with the variation in present-day cratering rates on the inner satellites of these three planets: The ratio for Saturn/Neptune/Uranus is roughly 3/50/100 (*39*). It would appear that where bombardment is greatest, there is less overall mass. However, the present-day differences in the distribution of mass around the giant planets may reflect, in part, the varying degrees to which bombardment and collisional processes have combined to shape their ring-satellite systems.

The presence and distribution of dust in these systems may provide a direct indication of the relative importance of these processes today. The relatively large number of microscopic particles spread throughout the Neptune rings (Fig. 20) is not unique; the Jupiter ring and the Saturn E ring contain a fractional optical depth of 50% to 80% in dust. However, the absolute abundance of dust in the Neptune system, which is about two orders of magnitude larger than the Jupiter and Saturn counterparts, presents a serious problem. Because microscopic particles are very short-lived (*40*), they must be continually replenished. When material is in a state of dynamic balance, equilibrium abundances are maintained by equal rates of creation and destruction.

Different removal processes dominate in different environments: In the Uranus rings, microscopic material is removed primarily by gas drag (*41*) and, in the Jupiter rings, by plasma drag (*40*). In the Neptune rings, in which dust has a relatively large optical depth (approximately 10^{-4}) and which are relatively free of plasma or neutral gas, simple sweep-up on the surfaces of macroscopic particles dominates dust removal.

If the source of the dust is meteoroid bombardment, as believed for the Jupiter ring, the creation and removal processes are both proportional to parent body optical depth. Consequently, the dust optical depth resulting from meteoroid bombardment is independent of the large particle optical depth and depends instead on the meteoroid flux and impact yield parameters (*40*). For heliocentric distances less than 15 to 20 AU observed by the Pioneer 10 and 11 dust detectors, a value of interplanetary meteoroid flux of about 10^{-16} g cm^{-2} s^{-1} is generally accepted. Given this value and ejecta yields of about 10^4 [see, for example (*42*)], "Jupiter ring" dust optical depths on the order of 10^{-6} are easily obtained. However, dust optical depths in N42 and the plateau (and the Uranus dust bands) are around 10^{-4} (Fig. 20), requiring a bombarding flux roughly two orders of magnitude larger than found at Jupiter and Saturn. This larger dust abundance is qualitatively consistent with the previously mentioned larger estimated projectile population at Uranus and Neptune. Although the estimate falls short by a factor of 3 to 10, this may be within the uncertainty in the Neptune dust optical depths and in the estimated projectile populations.

However, the dust within the N53 and N63 rings is orders of magnitude larger than can be explained by the meteoroid bombardment mechanism. Therefore, we suspect that it is most likely generated locally through vigorous collisions between larger, unseen particles. In this mode, the equilibrium dust optical depth depends in a more complicated and model-dependent way on the optical depth of the parent bodies that create it. The dust optical depth does tend to increase with that of the colliding parents as long as the latter is much less than unity and the mass injected per collision is a constant. This creation of dust through interparticle collisions, assuming relative velocities con-

sistent with radial excursions as large as the observed ring widths, may explain the generally large dust abundance in the Neptune rings, given reasonable assumptions about the yield per impact (*43*). The brightening at 57,500 km (1989N5R) near the outer edge of the plateau is one Neptune ring feature which, by analogy with Uranus, may be the manifestation of a moonlet belt (*1*). The lack of other noticeable fine structure, in contrast to the nearly 100 belts revealed in the Uranus rings or the internal structure of the Saturn D ring, may be due to long exposure times of the images and the corresponding smear rather than to actual absence. Of course, greatly increased optical depth will diminish the dust population because the attendant large collision rate tends to damp the relative velocities. For instance, in the large optical depth rings of both Saturn and Uranus, the dust fraction is extremely small. For this reason, it is not clear whether the amount of dust in the Neptune arcs is consistent with a relatively simple moonlet-belt model or whether additional stirring of the ring arc material by unseen perturbing bodies is implied. Nonetheless, it appears overall that the moonlet-belt hypothesis that has been proposed for the Uranus rings (*1*) and recently modeled in more detail (*44*) may go a long way toward explaining some of the global characteristics seen in the Neptune ring system.

While it seems clear that the 1989N1R arcs are stable over an interval of at least 5 years, a search for dynamical relationships between the Neptune rings, ring arcs, and the new satellites found within the ring region has demonstrated that none of the current hypotheses based on the combined action of satellite corotation and Lindblad resonances can explain the persistence of the arcs. Confinement of the ring arcs through a combination of corotational and Lindblad resonances with a single satellite (*27*) can be easily discounted on several grounds: (i) 1989N4 has zero inclination and eccentricity to within measurement uncertainties, thereby rendering it incapable of corotationally shepherding 1989N1R; (ii) the 3:2 corotation resonances of 1989N6 fall some 250 km outside 1989N1R, and the expected scale for this resonance (about 60°) is too large; (iii) the 5° inclination of this satellite is insufficient to allow it to confine a ring arc 15 km wide, given its radius of 27 km and a reasonable assumed density. The Lagrange point satellite shepherding model (*26*) can be discounted because no Lagrange point satellite of sufficient mass has been found. The only relationships that hold some promise for being significant are the standard outer Lindblad-type resonances of 1989N4 on the N63 ring and 1989N3 on the N53 ring, which might account for the locations of the inner edges of these rings in much the same way as Cordelia shepherds the inner edge of the Uranus ϵ and probably λ (1986U1R) rings (*45*). Though both inertial and acoustic waves in Neptune were proposed as a possible mechanism for the azimuthal confinement of arc material, these mechanisms can now be discounted because the required planetary wave amplitudes would have to be impossibly large to produce arcs with the observed longitudinal scale of 12° (*46*). Moreover, acoustic mode corotation resonances at Neptune do not fall outside 28,000 km (*47*). At the present time, therefore, there are no theories explaining ring arcs that are verified in Voyager imaging data.

The effort to date that has focused on the details of a longitudinal confinement mechanism for the arcs, while now clearly justified, does not address the larger question of the origin of rings and ring arcs themselves. This question will require studies of catastrophic disruptions and the subsequent dispersal and distribution of collisional fragments, as well as the study of the coupled behavior of ensembles of moonlets and ring material, both under the influence of a variety of ongoing processes, like tidal evolution and meteoroid bombardment, which continually sap orbital energy and angular momentum from the system. However, knowing as we do now the basic properties of the four ring-satellite systems of the outer solar system, we can begin to explore comprehensive models of their undoubtedly complex evolution.

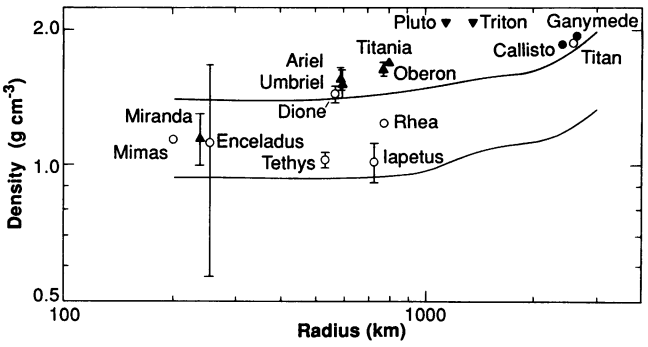

Fig. 22. Comparison of radius and observed mean density for outer solar system objects. Filled circles are satellites of Jupiter, open circles satellites of Saturn, triangles satellites of Uranus, and inverted triangles Pluto and Triton. The upper curve represents a simple compression model for a satellite with 60% water ice and 40% silicate (*53*); the lower curve is a pure water-ice model for comparison.

The Satellites of Neptune

Prior to the Voyager 2 encounter, Neptune's known satellite system consisted of one large retrograde satellite, Triton, a smaller satellite, Nereid, in a direct but highly eccentric orbit, and the tentatively identified satellite (*22*) in the vicinity of the ring arcs. Triton was discovered in 1846 by Lassel, immediately following the discovery of Neptune; Nereid was not discovered until the 20th century by Kuiper in 1949. Unsuccessful satellite searches using modern CCD cameras from ground-based telescopes placed upper limits on the diameters of additional satellites. These limits ranged from about 40 km at 15 Neptune radii (R_N) up to about 2000 km at 3 R_N (*48*). Of the six newly discovered satellites, two (1989N1 and 1989N2) were imaged with sufficient resolution to study their surfaces.

Its proximity to Neptune and low relative brightness make ground-based observations of Triton difficult; many of its fundamental properties (diameter, albedo, mass, atmospheric pressure) remained obscure prior to Voyager's encounter (*49*). Spectroscopic studies established the presence of methane (CH_4) ice or gas (or both) but showed no water-ice absorption features which are so prominent in the spectra of most outer-planet satellites. These studies also tentatively identified molecular nitrogen (N_2) in the gaseous and condensed states on the basis of a weak absorption band at 2.15 μm (*50*).

Triton's physical properties. Triton's radius (1350 ± 5 km), determined from limb measurements on the Voyager images, and mass, obtained from analysis of radio tracking data (*14*), yield a density of about 2.075 ± 0.019. With the exceptions of the rocky satellites Io and Europa, Triton's density is the highest observed for an outer-planet satellite and is very similar to that of the Pluto/Charon system; see Fig. 22 (*51, 52*).

If these bodies are assumed to be composed chiefly of silicates and water ice, the rock/ice mass fractions can be derived from the bulk density by using interior structure models (*53*). Two extreme cases are examined here: differentiated (silicate core and ice mantle) and homogeneous (uniform mixture of silicate and ice or clathrate). A silicate density of 3.361 g cm^{-3} was used (*54*); a "chondritic" value of 3.6, used in some other studies, would result in slightly lower silicate mass fractions than those quoted here.

In the case that Triton was melted and

Table 2. Triton interior model parameters, where P_c is the model central pressure in bars, X_{sil} is the silicate mass fraction (assuming a model uncompressed silicate density of 3.361 g cm^{-3}), and ρ_u is the model uncompressed density of Triton in grams per cubic centimeter.

	Silicate core Ice-I mantle	Silicate core Ice-I/Ice-II mantle	Undifferentiated Silicate + Ice-I + Ice-II
P_c	20360	20150	11290
X_{sil}	0.75	0.69	0.65
ρ_u	2.01	1.83	1.74

completely differentiated, it would have formed a silicate core approximately 1000 km in radius overlain by an Ice-I mantle approximately 350 km thick (Table 2, column 1). As the interior cooled, a layer of Ice-II may have developed due to the very low surface temperature. The existence and thickness of such a layer strongly depend on the details of the Ice-I/Ice-II phase boundary, poorly known for these low temperatures. Ice-II also will not be present if the ammonia hydrate/water eutectic is reached and some of the interior is partially molten. Column 2 of Table 2 gives the characteristics of models for a mixture of Ice-I and Ice-II by means of the phase relation given by Lupo (*54*). A homogeneous undifferentiated model (Table 2, column 3) would result in a layered structure of silicate mixed with Ice-I, Ice-II, and Ice-VI in the deep interior.

The differentiated models are clearly the most plausible. Triton is large enough that radiogenic and accretional heating alone likely resulted in differentiation. In addition, if Triton is a captured satellite, tidal evolution of its orbit also would have produced significant heating and melting (*55, 56*). Triton's extensive resurfacing is also inconsistent with an inactive, homogeneous interior.

Triton's estimated silicate fraction is higher than those of the large icy satellites of Jupiter, Saturn, and Uranus, but similar to that of the Pluto/Charon system; see Fig. 23 (*53*). This is consistent with the hypothesis that Triton was formed in the solar nebula and subsequently captured by Neptune (*55*). These high densities have important implications for the carbon chemistry of the outer solar nebula. If the nebular carbon were mostly in CO gas, the H_2O abundance would be depressed relative to that of the silicates (*53*). Modifications to the simple concept of CO-rich versus CH_4-rich nebulae may be required, however, in response to recently suggested revisions of the cosmic carbon abundance (*57*) and to the lack of detected CO on Triton or Pluto.

Another important aspect of these models is the relatively high interior temperatures expected, even at the current epoch. If conductive heat transport alone is considered, with the radiogenic heat produced by a 2000-km-diameter chondritic core, the eutectic melting point of ammonia hydrate would be reached at a depth of only 200 to 300 km; the melting point of water ice would be near the core-mantle boundary. Convective heat transport in sub-solidus convection would cool the interior more rapidly than conduction alone, and more complicated models need to be considered.

Local topographic relief on cliffs, ridges, knobs, pits, and craters commonly exceeds ~1 km over most of Triton's surface. This implies that a rigid material, which would not flow at the 40 to 50 K near-surface temperatures over billions of years, is required to support them. The rheologies of solid N_2 and CH_4 are not well known at these temperatures but it seems unlikely that a 1-km-high cliff could be supported over geologic time in a material held at half to two-thirds of its melting temperature. Such relief could easily be supported in water ice or water-dominated ammonia-water ice, however. We suspect that water ice is in fact the primary component of the near-surface crustal materials overlain by thin veneers of nitrogen and methane ices and their derivatives.

Triton spectrophotometry. Clear-filter, narrow-angle images acquired during the last 2 weeks of approach were analyzed to determine Triton's light curve (Fig. 24). Integral-disk brightness measurements were scaled to constant distance from Triton and corrected for the disk-averaged phase curve described below. Confirmed by preliminary geodetic control measurements, these data indicate synchronous rotation. A Cassini state 2 rotation state (rotation axis not perpendicular to the orbital plane) was suggested as a theoretical possibility based on dynamical arguments (*58*) but is ruled out by the data. The light curve agrees well in magnitude and sense (leading side brighter—90° longitude, Figs. 24 and 25) with broadband V filter measurements, but telescopic measurements at 890 nm show no light curve larger than about 2% (*59*). This suggests that the surface contrast at 890 nm is less than at visible wavelength and implies that the chromophores (possibly silicates or hydrocarbons or both) responsible for albedo and color variations on Triton are more absorbing at shorter wavelengths.

Triton was imaged at phase angles between 12 degrees and 156 degrees through the violet, green, and clear filters. These data are combined with ground-based V bandpass data (similar to the green filter in effective wavelength) in Fig. 26. Also shown are fits to the green and violet data using Hapke's photometric model; see (*61*) and Table 3. The phase curves display remarkable wavelength-dependent differences. At small phase angles Triton is brighter in the green filter than in the violet; at large phase

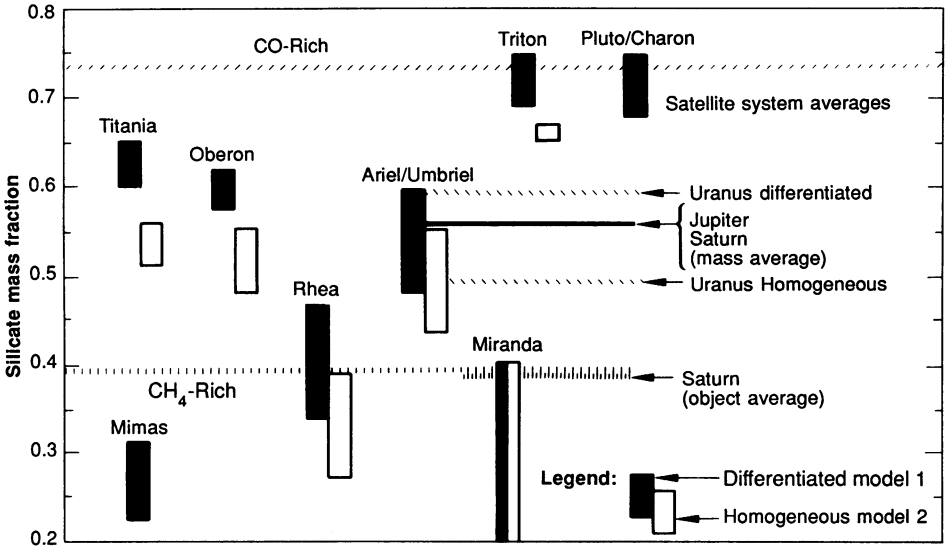

Fig. 23. Comparison of model silicate mass fractions for several outer planet satellites and the Pluto/Charon system (*53, 54*). Two types of satellite interior structure are given, a fully differentiated body with a silicate core and an ice mantle, and a homogeneous undifferentiated mix of water ice and silicates. Radiogenic heating is taken into account in the current thermal structure of the interiors. Also shown are approximate values for silicate mass fraction for bodies formed in CO-rich and CH_4-rich nebular conditions and the system averages from several satellites as compiled in (*51*).

Table 3. Triton photometric parameters. The V band value is from a ground-based measurement (*60*).

Filter	p	q	A	w	g	$\bar{\theta}$
Violet	0.61	1.5	0.90	0.999	+0.16	3°
Green	0.71	1.2	0.88	0.996	−0.22	5°
V	0.78					

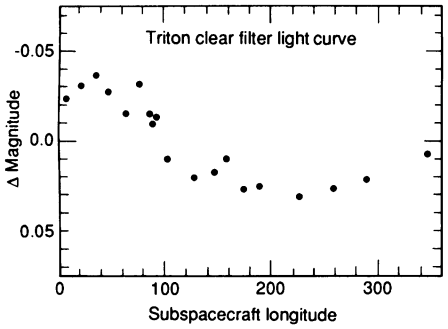

Fig. 24. Triton light curve. The disk-integrated brightness of Triton in arbitrary units normalized to a constant distance from Triton is shown as a function of subspacecraft longitude (in degrees). The data were derived from clear-filter narrow-angle camera. The period of revolution was assumed to be synchronous.

angles the reverse is true. Clear-filter data are intermediate.

At large phase angles (>150°) the violet- and green-filter data both deviate from the fitted Hapke functions, with the deviation being larger in the violet filter. This may result from the effects of atmospheric scattering at large phase angles, which are not accounted for in our models. Atmospheric scattering is expected to be greater at large phase angles and at shorter wavelengths. The more positive value of g (indicative of forward scattering particles) for the violet filter Hapke fit is consistent with the presence of atmospheric scattering.

Triton's global-averaged, single-scattering albedo is among the highest of the outer-planet satellites studied to date. Only values for Enceladus ($w \sim 0.998$) and Europa ($w \sim 0.97$) are comparable (*62*). The Hapke parameters can be used to estimate violet- and green-filter geometric albedos (p), phase integrals (q), and spherical albedos ($A = pq$). These values are given, along with the ground-based V filter value of p in Table 3. The greater-than-unity phase integrals are unusual for icy, airless satellites, but such values are expected for an object covered by transparent grains of frost or terrestrial snow (*63*).

The green-filter Hapke parameters were used to derive crude normal albedos for various regions imaged at high resolution through the green filter (Table 4). Green-filter data were chosen as they are less influenced by atmospheric scattering than are the violet data and because both ground-based and Voyager-imaging observations can be used to constrain global photometric parameters.

Figure 27A compares Triton color data derived from Voyager imaging observations with contemporaneous ground-based observations (*64*) and with ground-based observations acquired about a decade earlier (*65, 66*). The Voyager data were reduced to normal albedos by using the global-average phase function discussed above. Both the Voyager imaging and contemporaneous ground-based measurements of Tholen (*64*) show Triton to be substantially less red than indicated by the earlier ground-based observations. Because both the 1979 and the 1989 measurements have each been confirmed by two sets of independent observations, it is clear that Triton's global color changed in the intervening decade. This is not surprising. The subsolar latitude ranges between about 55°N and 55°S on time scales of several 100 years (*67*). Ground-based measurements indicate solid nitrogen and methane on Triton's surface and Voyager UVS observations show these compounds are dominant in its atmosphere (*50, 68*). These ices are quite mobile, even at the 37 to 39 K surface temperature of Triton. It is quite plausible that volatile transport, combined with the 10° change in the subsolar latitude between 1979 and 1989, could account for the large change in the disk-averaged color.

Comparison of the colors of several large albedo units and streaks (Fig. 27, B and C) reveals that the central polar unit is slightly reddish, similar in color to the dark streaks. The bright equatorial collar along the outer fringe of the cap is neutral and very bright, suggestive of freshly condensed frost. The redder areas may be contaminated with darker, redder material. The reddest areas measured are in the plains north of the bright collar that extend all the way to the terminator in the north. Even Triton's "darkest" regions are in actuality quite bright in comparison to most outer-planet satellites. Even the "dark" streaks show normal reflectances in the range of 0.40 to 0.75. Only a few small spots in the northern plains have normal albedos with values as small as ~0.20.

One explanation for Triton's reddish color is that the surface is dominated by a physical mixture or solid solution of methane in nitrogen and that organic polymers produced by photolysis and charged-particle bombardment of methane are responsible for the red coloration (*69*). Although alternative explanations do exist (for instance, that the coloring agent is derived from primordial organic material or from material that continues to accrete onto Triton's surface), it is certain (i) that methane is present on the surface and in the atmosphere and (ii) that methane will be polymerized by interaction with cosmic rays, UV photons, or charged particles, or all of these.

Triton's geologic processes and evolution. Voyager 2's highest resolution view of Triton was of the hemisphere that faces Neptune in synchronous rotation. Figure 28, the first

Table 4. Voyager green-filter normal albedos of Triton terrains.

Terrain	Normal albedo
Average dark polar cap	0.82 ± 0.03
Bright ice (polar cap edge)	0.88 ± 0.02
Bright polar frost	0.89 ± 0.02
Dark streaks	0.62 ± 0.04
Dark pond (centers)	0.76 ± 0.02
Dark pond (edges)	0.95 ± 0.04

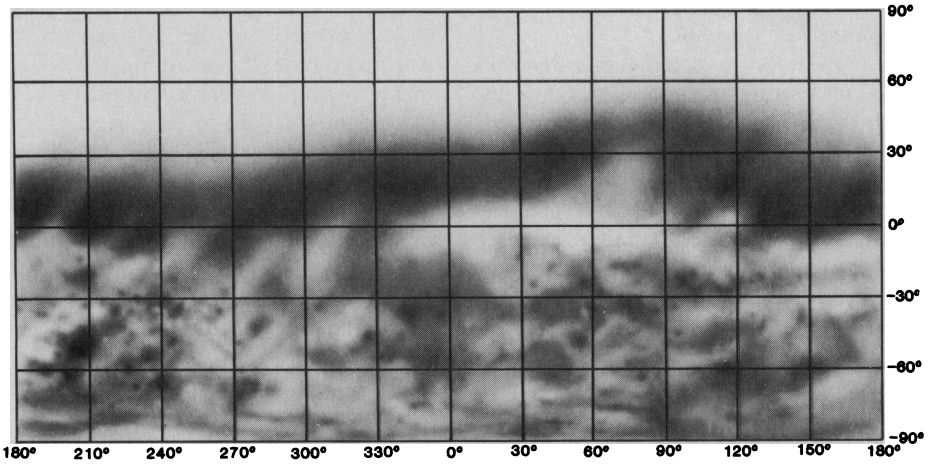

Fig. 25. Global map of Triton. The airbrush drawing shown here covers the 30° to 45°N to 90°S (+30° to −90°) region in cylindrical projection. It was drawn by J. L. Inge of the United States Geological Survey.

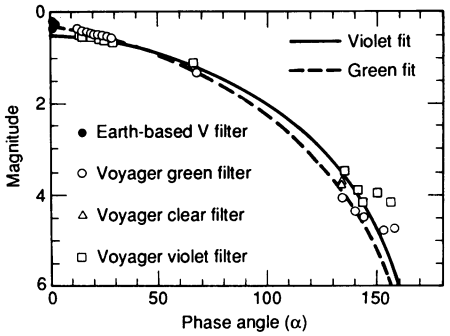

Fig. 26. Voyager camera violet-, green-, and clear-filter phase curve for Triton. Magnitude is normalized at zero phase angle to equal to $-2.5\log_{10}(p)$, where p is the geometric albedo. The solid line represents the best-fit Hapke parameters for the violet filter; the dashed line is for the green filter (see Table 3). Both curves assume $B_0 = 0$ (no opposition surge).

image to clearly show surface features, and Fig. 29, a mosaic of higher resolution mapping frames, both show this hemisphere. Less than 40% of Triton was imaged at high resolution; it should be kept in mind that our understanding of Triton's geologic processes and history is limited to this sample.

By comparison to most planetary surfaces, Triton's appears geologically young; like Io and Europa, heavily cratered terrains are absent. All other outer-planet satellites display regions of heavily cratered terrains that evidently date back to the early post-accretional bombardment. Triton's surface is consistent with an object that was geologically active and resurfaced well after the period of heavy bombardment.

Albedo patterns. Triton's color and albedo patterns can be broadly divided into (i) units of the brighter polar cap that occupy nearly the entire southern hemisphere and (ii) somewhat darker and redder plains that extend roughly from the equator northward to the terminator (Fig. 25). Data of Table 4 show that all of these surfaces have very high albedos (0.6 to 0.9); all are likely composed substantially of volatiles.

In most cases the color/albedo units do not correlate with geologic terrains or topographic features, suggesting they represent thin veneers draped over the terrain units (Fig. 30). For example, clusters of strange albedo patterns with irregular, rounded, dark centers surrounded by bright aureoles occur near the eastern limb (Fig. 30, lower right). A few impact craters can be seen near and on them but they themselves display no obvious topography. The interior of the polar cap displays discrete boundaries and irregular, patchy areas that appear to be "windows" in the bright reddish icy deposit (Fig. 30, lower left). There are no convincing cases of relief along these discrete edges, which is again suggestive of thin deposits below the limits of detection.

The slightly darker streaks scattered over the interior of the ice cap resemble the ubiquitous martian "wind streaks" attributed to eolian erosion and deposition. The Triton streaks range in length from a few 10's up to about 100 km. Often small, darker, irregular patches a few kilometers across occur at the heads of the streaks; less commonly a bright region also appears near the head. Although between roughly 10° and 30°S, the streaks are preferentially oriented toward the northeast; farther to the south the directions are highly irregular with streaks crossing one another. In a few cases streaks of opposite direction originate from the same point.

Whether the streaks are modern or ancient features is difficult to say from their surface patterns alone. It seems unlikely that they are older than very many Triton years (that is, a few thousand years), because the dark particles of which they are probably formed would migrate deep into the ice deposits after multiple cycles of pole-to-pole migration of the volatiles.

Transport of material by the winds in Triton's tenuous atmosphere seems required as part of the explanation for the streaks. As mentioned earlier, some methane will inevitably be converted to particles of dark complex hydrocarbons that will be found in Triton's surficial deposits. Those particles that are fine enough (a few micrometers or less) can be suspended in the atmosphere and carried substantial distances downwind. For Triton dust settling occurs in the Epstein or kinetic regime as opposed to the Stokes or viscous regime as the mean free path in the tenuous nitrogen atmosphere is large compared to the particle size. From simple momentum transfer arguments, we estimate, for instance, that a 1-μm particle would settle through the bottom scale height (about 14 km) in about 5 days. The basic question is how the dark particles become airborne in the first place. The estimated threshold velocity for the surface wind to pick up particles a few micrometers in diameter could be as low as roughly 1 ms^{-1}. Such surface winds are quite conceivable. As discussed below, however, at least two dark geyser-like plumes have been identified. In one, dark material is clearly erupting nearly vertically to an altitude of about 8 km. Purely eolian explanations are not required unless the dark streaks are polygenetic.

Morphological units. The topography of the central part of polar cap (br, bs, bst in Fig. 31) is difficult to interpret owing to the exceedingly complex albedo patterns. Only a few inarguable topographic landforms can be distinguished in those units, all impact craters. Our descriptions of Triton's surface morphology are confined to the terrains to the north (Fig. 31).

An extensive unit termed the "cantaloupe" terrain (ct) dominates the western part of the equatorial region. It consists of a dense concentration of pits or dimples that are crisscrossed by ridges of viscous material

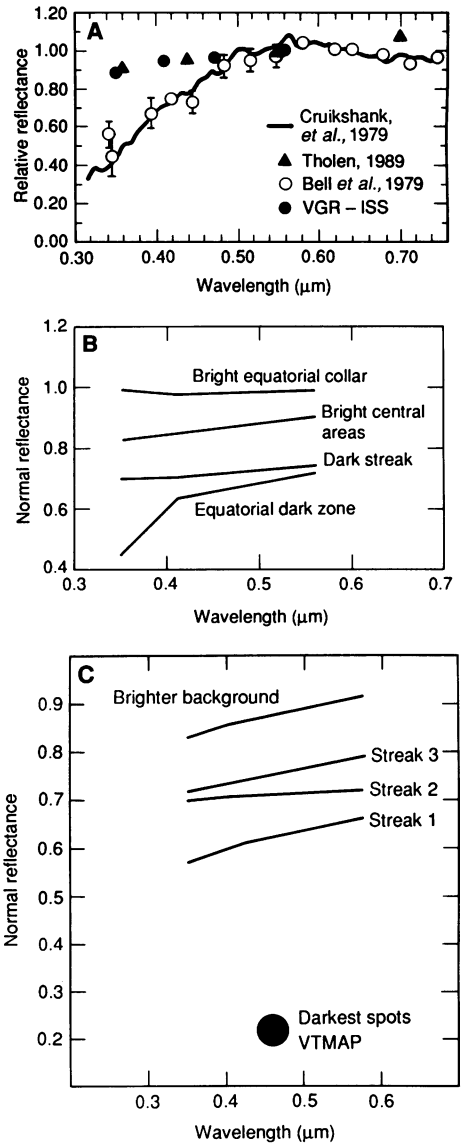

Fig. 27. Triton colors and albedos. (**A**) Ground-based spectra of Triton in the visual and near infrared taken in 1979 as well as contemporaneously with the Voyager encounter of Neptune are shown (*64, 65*). Plotted with the ground-based data are the Triton disk-averaged colors as obtained from Voyager narrow-angle camera images. Note the substantial color change from 1979 to 1989 shown by these data. (**B**) Normal reflectance of selected areas on the encounter hemisphere of Triton are shown (see text). (**C**) Normal reflectances of selected dark areas on Triton are shown. The brighter background spectrum is an average of bright areas adjacent to the dark streaks whose normal albedos are also plotted. The darkest spot is located north of the equator in the darker, redder plains.

erupted into grabens. The grabens are global in scale and organization, continuing into other terrains to the east and south. Most of the dimples fall into two roughly uniform size classes of about 5-km and 25-km diameter; the smaller ones are found dominantly in the western part of the terrain. Both sizes are often organized into linear, equally spaced sets. It is possible that none of these features is of impact origin. In fact, recognition of any impact craters in the cantaloupe terrain is extremely uncertain. Seen at the highest resolution (Fig. 30, upper left) the cantaloupe terrain displays an extremely rugged and mottled texture. Some combination of viscous flow and collapse and deterioration of the landforms by extensive sublimation of surface materials may have been responsible for the complex landscape observed here.

A morphological sequence in the degree of eruption into the grabens can be discerned. The sequence begins with the U-shaped floor at the Y-shaped branch in the top of Fig. 30, lower left. Farther northwest along the valley floor, a narrow ridge is visible that erupted along a section of the valley floor and along an intersecting fault, crossing out into the plains to the south. Even farther north in the cantaloupe terrain and to the east limb along the equator, viscous material welled up in the valley floors forming ridges that stand above the adjacent plains (Fig. 29).

In contrast to the cantaloupe terrain, the eastern plains are dominated by a series of much smoother units. The first of these is the floor material (sv) in two "lake-like" features a few hundred kilometers across located near the terminator (Figs. 29 and Fig. 30, upper right). The floors are extremely flat compared to other plains units, embaying the scarp-rimmed margins and surrounding numerous hills and knobs that protrude through the deposit. The floors are terraced, occurring at several levels separated by scarps a few hundred meters high, suggesting multiple episodes of emplacement. A cluster of small irregular pits surrounding a large central pit, likely associated with an eruptive vent, is found in each of the floors. A single impact crater about 15 km in diameter shows that material that is rigid on geologic time scales makes up the bulk of the floor material.

Another smooth plains unit dominates the region just south of the two flat-floored lake-like depressions. It occurs as high-standing smooth plains (sh) that appear to have erupted from large quasi-circular depressions; one can see that strings of irregular rimless pits occur commonly in this unit (Fig. 31). Like the flat-floored deposits, the high-standing plains are quite smooth and have a very low density of superimposed impact craters. In contrast, however, these deposits stand as thick masses extruded onto and standing above preexisting terrains. The deposits terminate with rounded flow margins partially burying subjacent landforms. In places these deposits appear to be a few kilometers thick. Eruptions of comparable style, recognized on Ariel, are thought to have been formed by highly viscous material, such as partially crystalline ammonia-water mixtures (*70*).

The third plains unit in the eastern region is a hummocky plain (th). It appears to have been formed by extensive eruption of material along sections of the grabens that flowed out onto adjacent plains forming hummocky, rolling deposits and obliterating sections of the graben entirely. Figure 29 shows this unit to have the greatest abundance of impact craters.

In general, Triton's global fault system evidences a tensional regime. Several features in the transition zone between the lake-like features and cantaloupe terrain, however, suggest lateral displacement along strike-slip faults. Some show an offset of a few kilometers, others up to 30 km. The best example is an irregular depression 100 to 120 km (Fig. 32, left). It resembles many other depressions so common in this region; by contrast its margins appear to have been offset along ridge-and-groove lineaments. We speculate that the feature was deformed by two subsequent strike-slip motions, each with an amplitude of about 30 km. When the image is sheared along the hypothesized fault lines, the outline of the feature is restored to one typical of other cantaloupe depressions (Fig. 32, right). Other truncated features also appear to line up after restoration.

Impact crater abundances and relative ages. At the resolution of the global mapping images of Fig. 29 (1.5 to 3 km per line pair) impact craters are generally rare. Craters with diameters from the limit of resolution up to about 12 km display sharp rims and bowl-shaped interiors. Larger craters, ranging up to the largest (27-km diameter) are complex, having flat floors and central peaks. The transition diameter from simple to complex and depth/diameter ratios for Triton's craters are similar to those observed on other satellites whose crustal materials are thought to be dominantly water ice. Ejecta blankets are not visible, probably due to inadequate resolution. The craters also do not have rays, probably because veneers of mobile surface volatiles mask them.

Impact crater statistics were collected for four areas (Fig. 33, top). Area 1, the most heavily cratered region, occurs in the leading hemisphere of Triton's rotation-locked, synchronous orbit. Area 2, the least cratered, coincides with units sv and sh. Area 3 is in the cantaloupe terrain. Area 4 is a part of the ice cap interior. Owing to difficulty of recognizing impact craters with any confidence, crater statistics for the cantaloupe terrain have been excluded.

Figure 33, bottom, compares the crater-size frequency distribution for areas 1, 2, and 4 with those of the lunar highlands, typical lunar maria, and the fresh crater population on Miranda's rolling cratered plains (*1, 71*). Triton's most heavily cratered terrain displays a population similar to that

Fig. 28. Color image of Triton acquired at a range of 530,000 km with a resolution of 10 km per line pair. Narrow angle images obtained with green, violet, and ultraviolet filters were used as the red, green, and blue components. High frequency information from a clear image, containing the greatest detail, was merged with the color data.

of the lunar mare. Because the statistics of the population are so poor, all we can really say is that the range in crater density between the oldest and youngest terrains is in excess of roughly a factor of 3.

Area 1, the most heavily cratered region, is in the leading hemisphere. Because Triton is retrograde, both impacting debris external to the Neptune system and that in prograde orbits within the system preferentially crater Triton's leading hemisphere. The cratering flux will display a systematic decrease away from the apex of orbital motion. Estimating relative ages from impact crater abundances on widely separated terrains could lead to erroneous results if this effect is not taken into account. However, the decrease in flux from area 1 to 2 would be much less than a factor of 2; the large difference in crater population must reflect a real difference in absolute age. If the cratering rate has been roughly uniform during the time that these populations formed, then it follows that these two terrains differ by at least a factor of 2 in absolute age.

In order to detect such a leading-trailing variation in the populations, statistics were collected for the areas denoted by dashed lines in Fig. 33, top. The approximate bounding longitudes and abundances per million-square-kilometer of craters with diameter >4 km, respectively, are 60° to 75°E: 13; 30° to 60°E: 12; and 0° to 300°E: 6. These statistics are broadly consistent with the expected factor of 2 decrease in crater density between the leading edge and

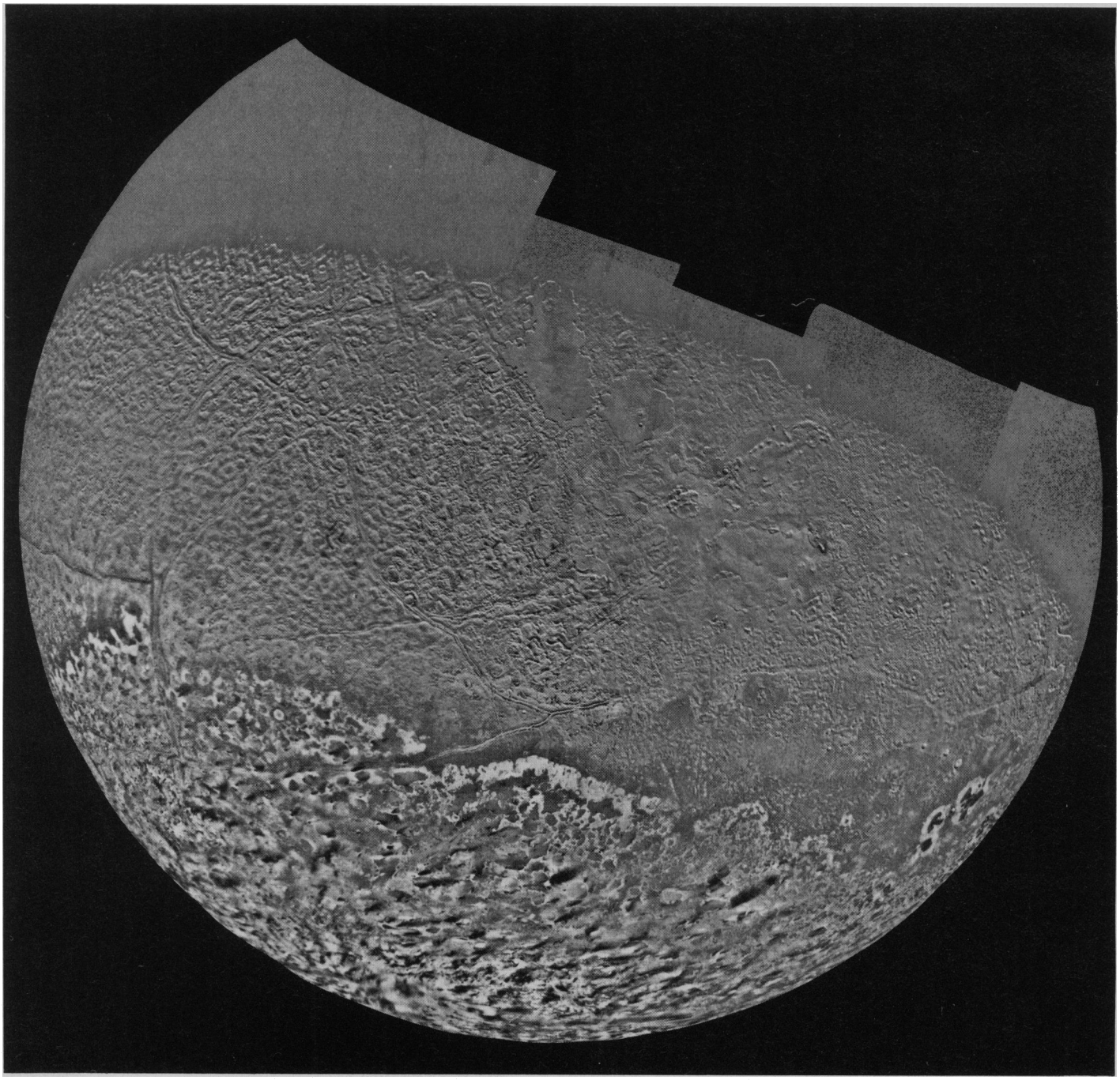

Fig. 29. Photomosaic of Triton. Centered in the Neptune-facing hemisphere at 15°N, 15°E, this orthographic projection was assembled from 14 individual frames with resolutions ranging from about 1.5 to 3 km per line pair. The mosaic has been high-pass-filtered to remove the gradient from bright limb to terminator in order to enhance surface detail over a wide range of normal albedo and lighting conditions. [Image processing by K. E. Edwards, E. M. Eliason, and J. D. Swann]

the boundary between the leading and trailing hemispheres.

Triton clouds and hazes. Despite the very low pressure, hazes and clouds can form in Triton's atmosphere from photochemical and condensation processes. The partial pressures of nitrogen and methane (*68*) are controlled by vapor pressure equilibrium with surface ices. Both gases should follow saturation vapor pressure curves in the troposphere, where temperature decreases with increasing altitude (*14*) and discrete condensation clouds of nitrogen ice were to be expected. Also, methane gas is dissociated by solar UV radiation, and subsequent chemical reactions will convert it into higher-order hydrocarbons, such as ethane and acetylene. Widely distributed hazes showing little structure, formed from these materials, were also expected (*72*).

A variety of atmospheric features are in

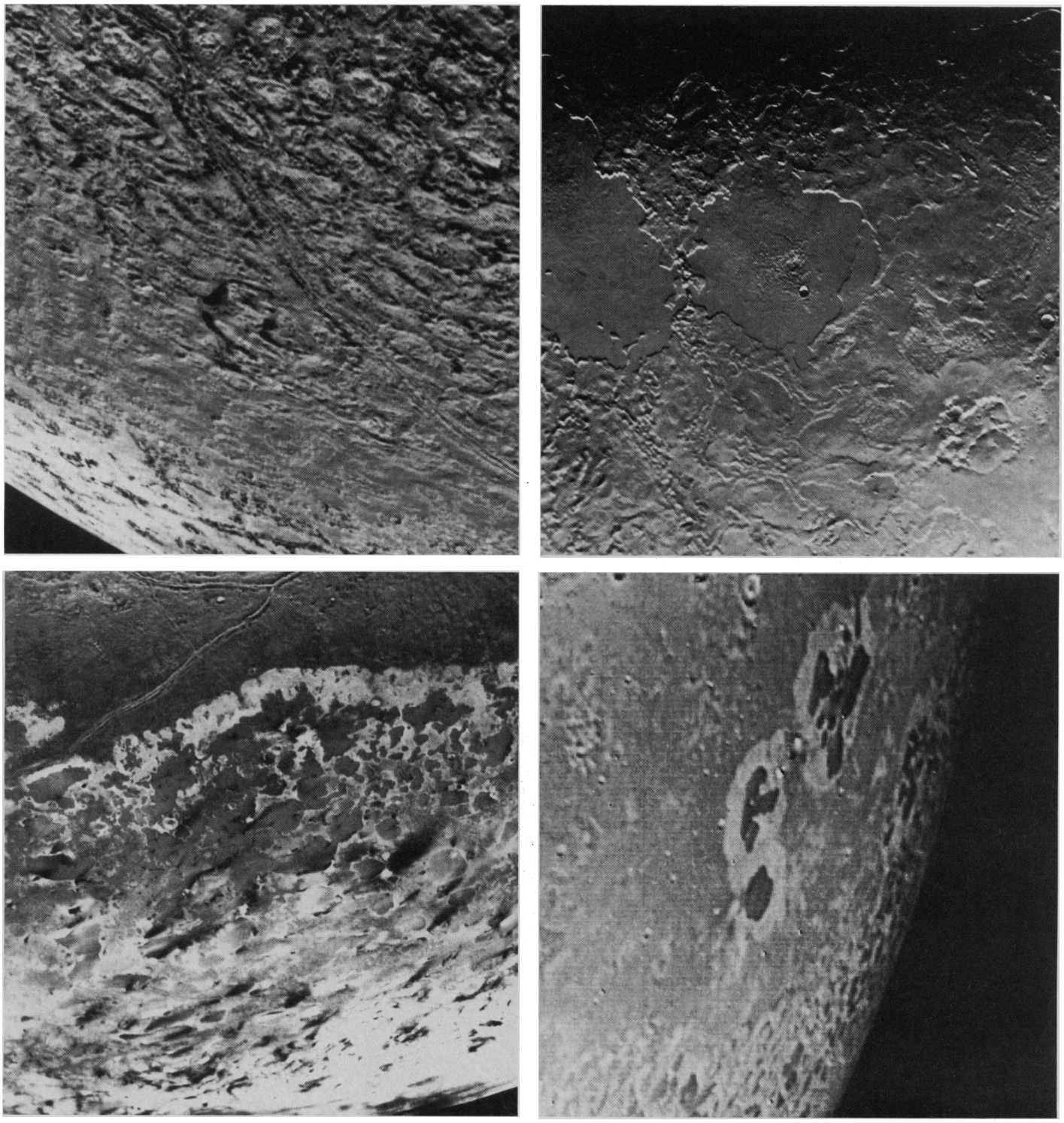

Fig. 30. High-resolution views of Triton's surface features. (**Upper left**) The complex surface texture of the cantaloupe terrain is shown with a resolution of about 0.8 km per line pair. [Image processing by E. T. Runkle] (**Upper right**) Smooth plains farther east are displayed at a resolution of about 1.5 km per line pair. (**Lower left**) The complex margin of the inner zone of the south polar cap is shown at a resolution of about 3 km per line pair. [Image processing by D. N. Jensen] (**Lower right**) Peculiar irregular markings with bright aureoles mark the edge of the inner cap zone in this view with a resolution near 3 km per line pair.

fact seen in the Triton images. These include clouds above the limb and extending into the terminator and an extensive optically thin haze that appears to be uniformly distributed around the disk. The haze is difficult to detect in limb images due to scattered light from Triton's bright surface, but it is easily seen in crescent images where it shows an extension of the cusp beyond the terminator. It apparently extends to an altitude of about 30 km, more than two scale heights, and has an optical depth of about 2×10^{-4}. We interpret it to be composed of photochemically generated smog-like particles described above.

Several clouds are seen in backscatter above both the east and west limbs (Fig. 34). In places these clouds are clearly detached; in others they appear to extend to the surface. The limb clouds appear above diffuse bright regions seen on the limb, suggesting that they are composed of bright particles that can be seen both in backscatter as well as in projection against the disk. All of the limb clouds so far detected are located over the subliming south polar ice cap. Brightness scans perpendicular to the limb

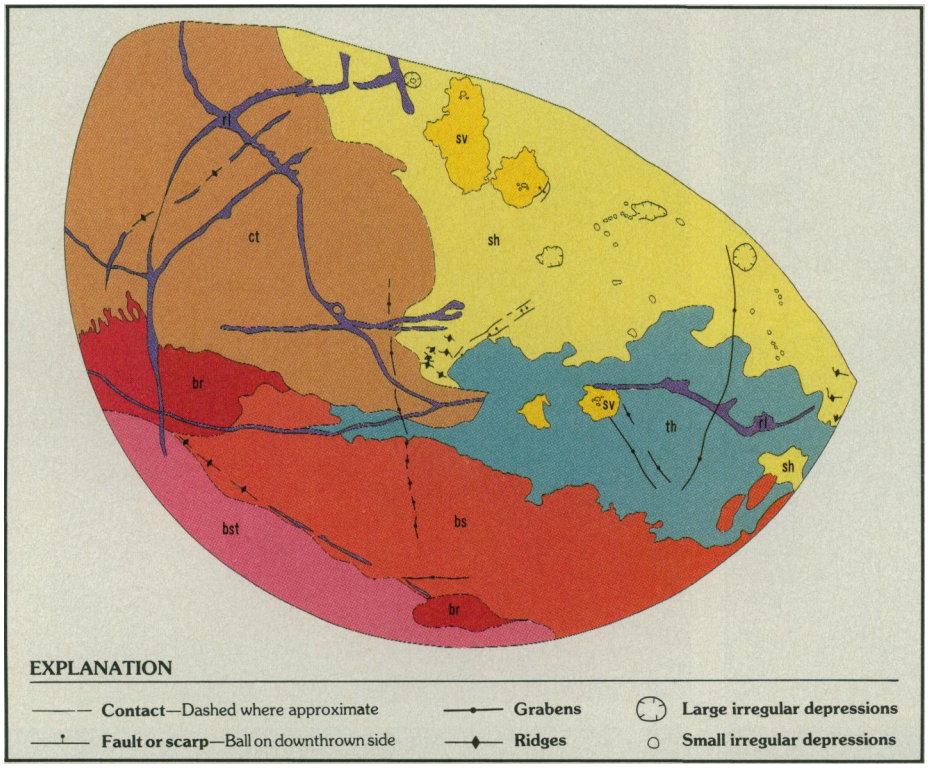

Fig. 31. Sketch map of Triton's terrains and south polar units. Units mapped are as follows: cantaloupe terrain-ct, smooth floor material-sv, high-standing smooth materials-sh, hummocky rolling plains-th, linear ridge materials-rl, bright spotted polar unit-bs, bright streaked polar unit-bst, bright rugged polar unit-br.

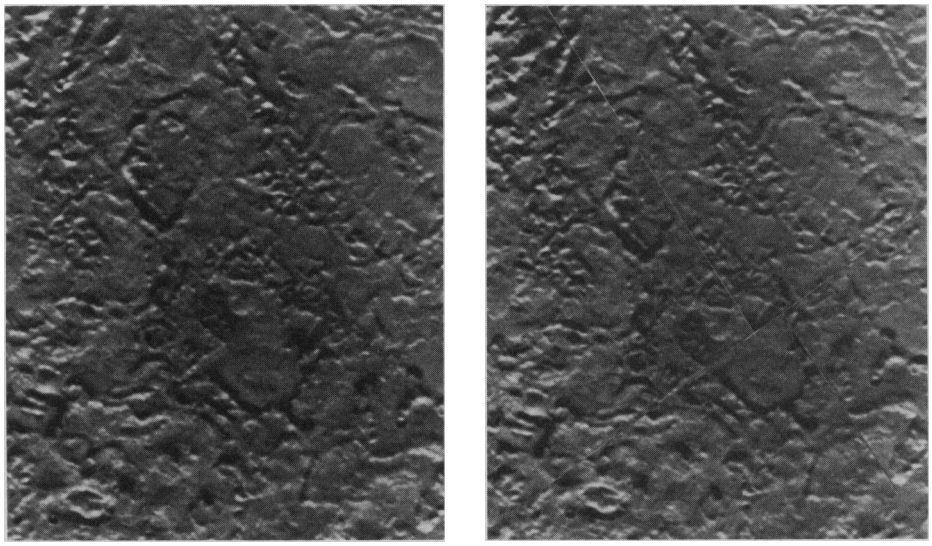

Fig. 32. Possible strike-slip faulting on Triton. (**Left**) The irregular depression near the center of the view appears to have been distorted by lateral faulting. (**Right**) One possible reconstruction of the feature shown in this view requires two episodes of strike-slip faulting, each with roughly 30 km of displacement.

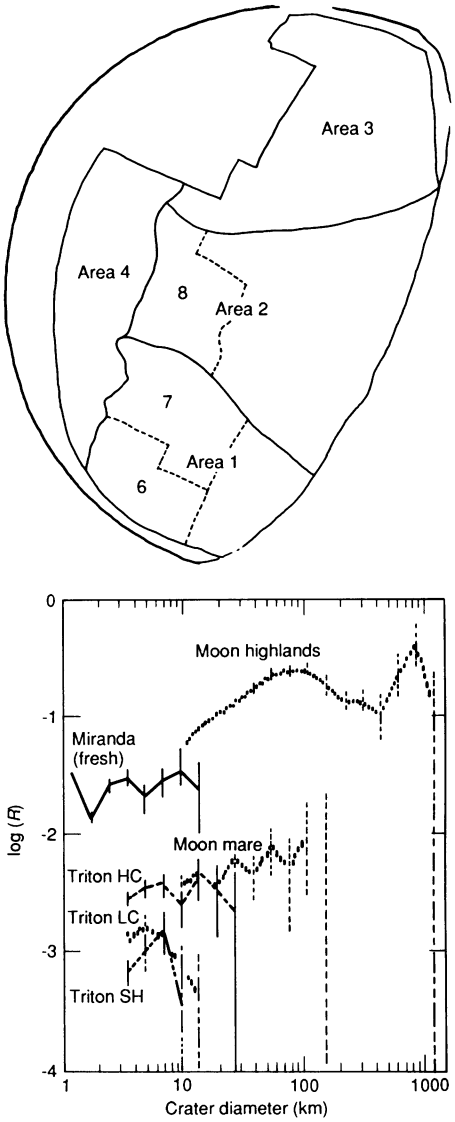

Fig. 33. Impact crater statistics for various regions of Triton. (**Top**) The locations of regions for which data were collected include: area 1, the most heavily cratered; area 2, lightly cratered; area 3, cantaloupe terrain, and area 4, a plains region just outside the inner cap zone. The dash-enclosed areas (6, 7, and 8) were analyzed to detect a possible gradient in the crater flux (see text). (**Bottom**) Triton crater size/frequency distribution for area 1 (Triton HC), area 2 (Triton LC), and area 4 (Triton SH) compared with the fresh crater population on Miranda, the lunar highlands, and the lunar post-mare. The curves were normalized to a standard −2 cumulative distribution power law as in (*1*).

on one of these images (Fig. 35) show a cloud that extends from close to the surface to an altitude of about 4 km, above which its brightness sharply decreases. We interpret this feature to be a nitrogen condensation cloud. The ubiquitous diffuse haze can barely be discerned in the scans extending from the surface to an altitude of almost 30 km.

Because they are thin, the optical thickness of the limb clouds can be estimated from their observed brightness. Assuming isotropic scattering (both of the direct and surface-reflected sunlight), we estimate optical depths of about 10^{-3}. If more realistic particle phase functions are used, the estimated optical depths are several times larger (*73*). Also, in some cases the brightness of the discrete clouds is as much as three times larger than shown in Fig. 35. Together these factors imply optical depths ranging up to 10^{-2}.

Bright clouds extending beyond the terminator are visible in a long sequence of outbound images of the opposite hemisphere to that seen in the mapping coverage (Fig. 36). The terminator is at roughly 45°S; again the clouds are seen above the south polar cap. From the distance they extend beyond the terminator, their altitudes are estimated to be in excess of 13 kilometers. These clouds remained stationary relative to the surface for the 2-day period as they rotated through the terminator region. They appear to correlate with dark surface markings seen in the low resolution approach images 3 days prior to closest approach.

Several east-west, elongated clouds can also be seen over the illuminated part of the crescent in a color image set acquired soon after Triton closest approach at a phase angle of approximately 140° (Fig. 37). Both clouds and surface detail can be discerned. The clouds apparently cast shadows, giving a very rough estimate of their altitudes of a few kilometers. Like the clouds associated with the geyser-like plumes described below, these elongated clouds are roughly 100 km long and 10 km wide. They may also be associated with erupting plumes, but no direct evidence exists for plumes connecting them to surface sources.

Triton's geyser-like plumes. The Voyager 2 images of Triton were acquired over a sufficiently wide range of viewing angle that many regions can be studied stereoscopically. The last global view of Triton, acquired just prior to closest approach to Neptune, was imaged from a sub-spacecraft latitude of about 15°S. Subsequent higher resolution frames of the mapping coverage were acquired from latitudes ranging from about 10° to 25°N at about the same longitude. Through stereoscopic examination and by projecting these images to a common perspective onto a sphere, it was possible to study topographic landforms and search for material aloft. In this way two active geyser-like plumes have been confidently identified; several others are suspected. All are located well inside the complex central zone of Triton's south polar cap.

The first of the two well-observed plumes (termed here the west plume) is situated at 334°E, 50°S (Fig. 38, top). West plume is visible in at least four views, which have emission angles of 37°, 62°, 67°, and 75° at its location. The feature appears as an 8-km-

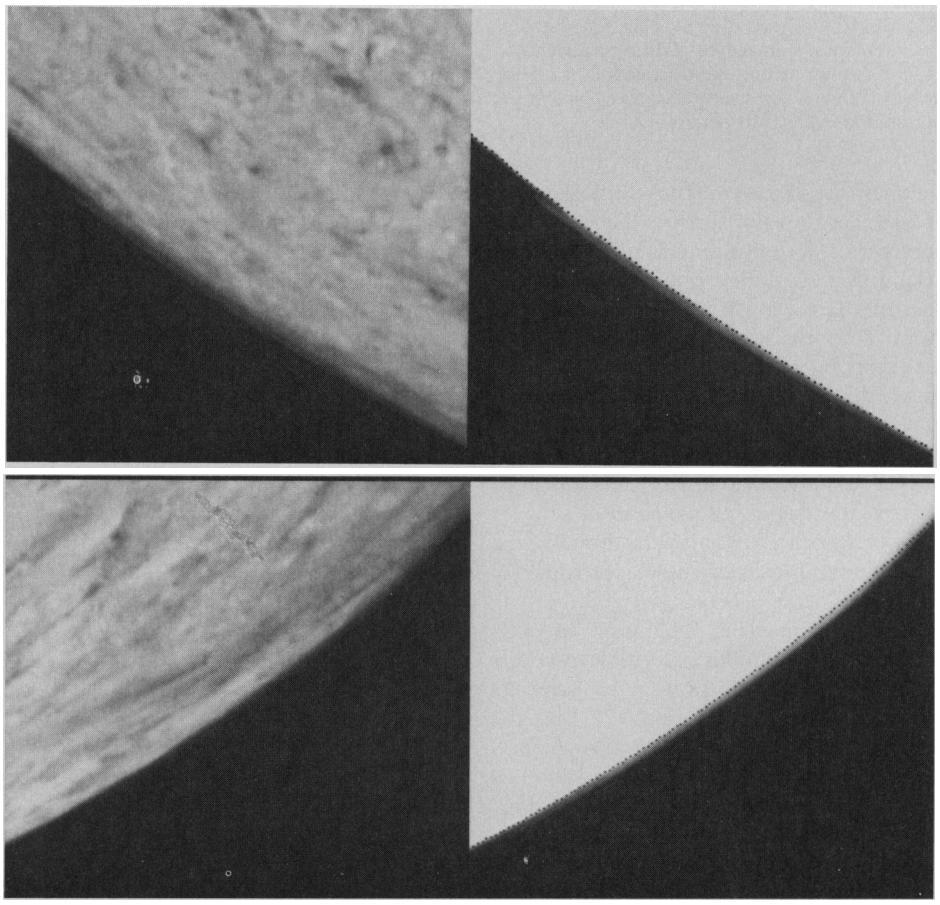

Fig. 34. Limb clouds above Triton's south polar cap. Each of the images is shown with two different stretches to enhance the limb clouds and surface features separately. Dark pixels mark the best estimate of Triton's limb. (**Top**) Cloud on the west limb that extends about 100 km along the limb and appears detached over much of its length. (**Bottom**) Cloud imaged above the east limb that extends about 200 km along the limb and is asymmetrical.

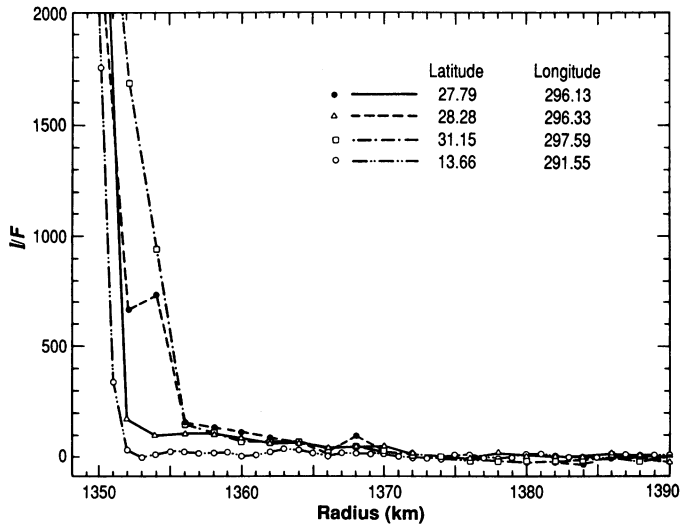

Fig. 35. Brightness scans across sections of the cloud shown in Fig. 34, top. The latitudes and longitudes of the scans are indicated.

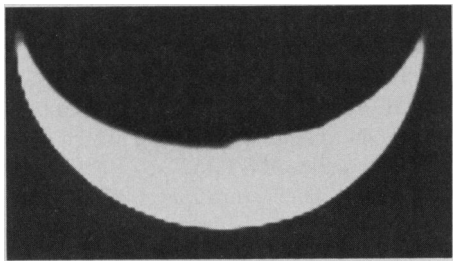

Fig. 36. Clouds extending over the terminator in an overexposed image of Triton's crescent acquired during the outbound sequence. The hemisphere shown is that facing away from Neptune at a resolution of 20 km per line pair.

tall narrow, dark stem rising vertically from a dark spot on the surface; the upper end terminates abruptly in a small dense dark cloud. A more diffuse cloud, appearing as a narrow dark band, can be seen extending westward for at least 150 km in the highest emission angle view, at which point it diffusely disappears. The cloud band maintains a very narrow projected width (approximately 5 km) along its length. In the later, higher resolution and higher emission angle images, the shadow of the band of cloud is visible; the sun was nearly directly above the west plume (incidence angle approximately 10°).

The east plume (Fig. 38, bottom) is located at 12°E, 57°S, and is also visible in at least four views with emission angles near the plume of 53°, 72°, 76°, and 77°. Like the west plume, it rises to an altitude of about 8 km where a small, dark, dense cloud is formed. In contrast to the west plume, however, its dark cloud of material is generally denser and diverges as it extends westward. The cloud is also quite dense in the vicinity of the source. Hence, although the rising column appears to be tilted slightly westward, its geometry is less obvious than in the case of the west plume.

In both cases the plume material rises roughly vertically to the 8-km altitude before being carried downwind. The geometry suggests stratification of the atmosphere may be controlling the form. Perhaps the 8-km altitude represents an inversion at the tropopause; as the plumes rise under some combination of momentum and buoyant force, they cease to rise above this altitude. The cloud geometry also suggests vertical structure in the wind speeds, in which the winds aloft increase abruptly at this altitude, although this clearly depends on the timescales for rising, suspension, and downwind transport.

It seems likely that the active dark plumes are related to the ubiquitous dark streaks scattered over the south polar region described earlier. The observed variation in the two plumes in terms of cloud density and degree of divergence is consistent with the variance seen in the collection of dark streaks.

Most plausible mechanisms to drive the plumes involve the venting of some gas from the surface, entraining fine dark particles. The particles are carried by some combination of ballistic and buoyant forces to altitudes where they are left suspended in the thin atmosphere to be carried downstream by the complex, sublimation-driven winds. The most likely driving gas is nitrogen, although models involving concentrated methane gas rising buoyantly are conceivable. Secondly, different types of energy sources can be considered, including insolation and geothermal energy sources either localized, for instance by intrusion of cryogenic lavas into areas of volatile material, or more broadly distributed through Triton's overall radiogenic heat flow. The fact that the active plumes are near the current subsolar latitude argues for a solar-driving mechanism. We discuss here one model out of many conceivable, simply to demonstrate

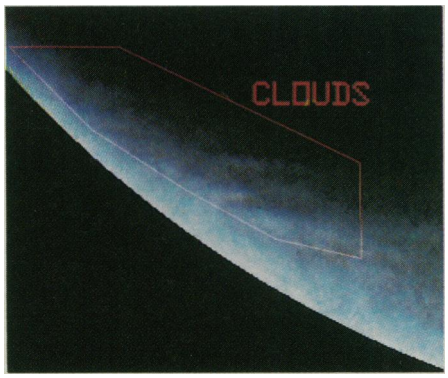

Fig. 37. High phase-angle image of Triton showing surface features and elongated clouds (to the left) evidently casting shadows near the terminator. In this view the resolution is about 9 km per line pair, the phase angle about 140°, and the subspacecraft position was centered at 208°E near the equator. Green-, clear-, and violet-filter narrow-angle images were used as the red, green, and blue components. [Image processing by T. L. Becker]

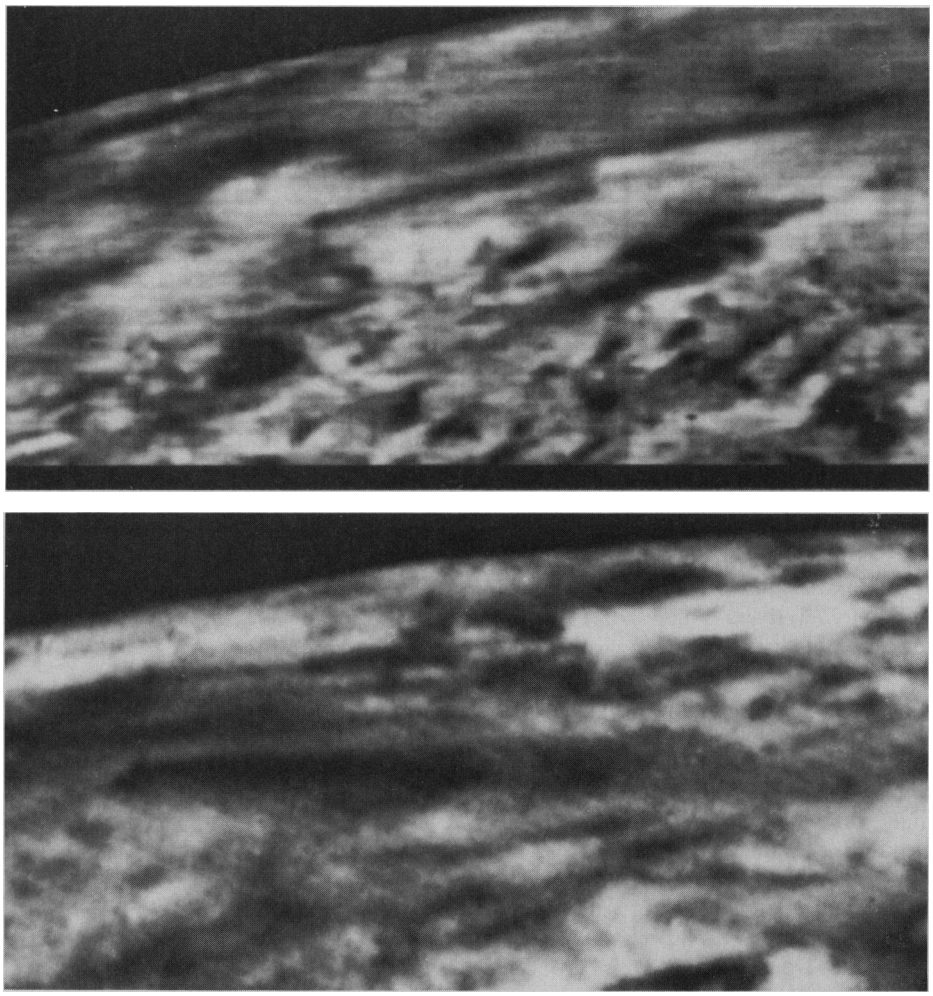

Fig. 38. Profile view of Triton's active geyser-like plumes. These two high-emission-angle views are of the regions near the southern limb; south is up, west to the right. In both views the spacecraft was about 15° above the horizon as seen from the base of each plume near its source. The plumes are about 8 km tall; the east-west dimension of the two views is about 150 km. The west plume is shown in top image; the east plume in the bottom image.

that simple, plausible explanations do exist. The model we describe is for solar-driven nitrogen gas geysers.

The insolation-driven mechanism involves a "greenhouse" effect. A way to construct an extremely efficient greenhouse is to cover a dark absorbing layer with a relatively transparent layer, which we propose to be a layer of nitrogen ice, that is both volatile and has a low thermal conductivity. Ground-based spectroscopic observations of Triton show an absorption feature at 2.15 μm that was attributed to nitrogen, requiring a path length in the nitrogen equivalent to a meter or more of solid or liquid (*50*). In this model the radiation is absorbed in a dark substrate beneath the nitrogen layer. The temperature will rise until the thermal gradient reaches a point where the excess heat is conducted and reradiated back to the surface.

The vapor pressure of nitrogen ice increases rapidly with increasing temperature. A temperature rise of 10 degrees above Triton's 37 K surface temperature results in roughly a one hundred-fold increase in pressure. If the layer of nitrogen is thick enough (>1 or 2 meters), sufficiently transparent, and locally seals off the subsurface, the subsurface vapor pressure will increase, filling permeable subsurface reservoirs. If the seal is ruptured or if the pressurized gas migrates laterally to an open vent it will rapidly decompress, launching a plume of nitrogen gas and ice, entraining dark particles encountered in the exit nozzle, and carrying them to altitude.

Small satellites. Of the newly discovered satellites (Table 1), only 1989N1 and 1989N2 were well enough resolved to see surface features (Fig. 39). As resolution was sufficient to measure radii directly for 1989N1, 1989N2, and 1989N3, their albedos are also reasonably well determined. One color sequence acquired of 1989N1 shows it to have a flat spectrum; violet-, green-, and clear-filter albedos all fall within 10% of each other, similar to Voyager photopolarimetry observations for 1989N2 (*29*).

The low resolution view of Nereid provided only an approximate albedo; no surface or limb features were detectable (Fig. 41). Nereid's spectral reflectivity (geometric albedo in the violet, green, and clear filters) is flat within 10%. Clear-filter images used to derive Nereid's phase curve between 25° and 55° (Fig. 40) yield a linear phase coefficient of 0.021 magnitudes per degree. No rotational effects were detected in the Nereid images; the amplitude of its light curve is less than 10%. Inasmuch as the orientation of Nereid's pole is unknown, we cannot derive limitations of its shape from these data. The Voyager viewing direction differed only by approximately 25° from that of recent ground-based observations (*74*) that suggested a large amplitude light curve. We see no evidence for an amplitude of more than 10%. The rotation period remains unknown.

1989N1 and 1989N2 are irregularly shaped; 1989N1 displays craters, one near the terminator about 150 kilometers across. 1989N1 was resolved at several longitudes and is slightly elongated; topography of about 20 km can be seen on its limb. The closest view weakly shows linear features; no substantial albedo features are seen. The irregular shape of 1989N1, which had a diameter of 400 kilometers, might seem surprising. However, the internal strength required to support such topography falls within the expected range even for an icy object (*75*).

Collisional histories of satellites. Bombardment by comets over the last ~3.5 billion years probably accounts for most of the craters observed on Triton and for the origin of the small satellites 1989N5 and 1989N6 by collisional fragmentation. The comet flux close to Neptune is dominated by comets captured into relatively short-period Neptune-crossing orbits by encounters with that planet. A rough estimate of the number of these Neptune family comets can be made by extrapolation from the observed Jupiter family of short-period comets (*76, 77*). On the basis of theoretical studies of the capture process (*78*), we infer that there is a fairly steady population of the order of a million Neptune family comet nuclei with absolute B-magnitude greater than 18 (this corresponds approximately to diameters greater than about 2.5 kilometers). This estimate is conservative; if most short-period comets have been derived from a region lying a moderate distance beyond Neptune or between Uranus and Neptune (*79*), the population of Neptune family comets might be 10 to 20 times higher. Long-period comets also strike the satellites of Neptune, but their impact contributes, at most, only a few percent to the estimated production of craters on Triton and on the small regular satellites.

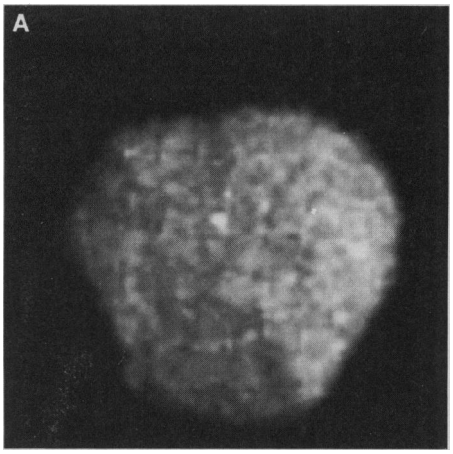

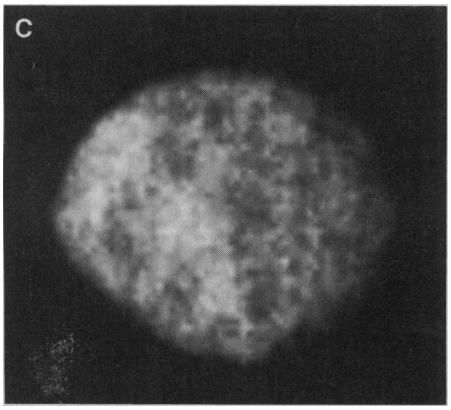

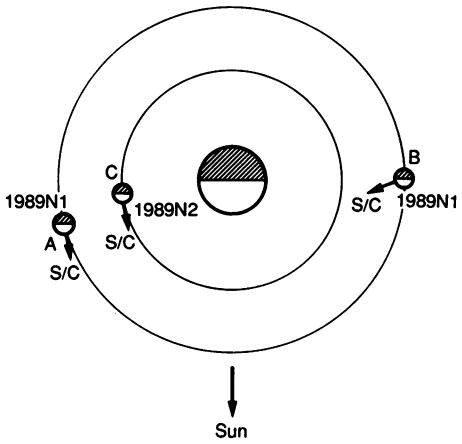

Fig. 39. Voyager 2's best views of 1989N1 and 1989N2. (**A**) 1989N1 is shown in this image at a resolution of 7.9 km per pixel; (**B**) 1989N1 is at 1.3 km per pixel; and (**C**) 1989N2 at 4.2 km per pixel. (**D**) Schematic of the viewing geometry. Arrows labeled S/C indicate spacecraft view; letters correspond to images A, B, and C.

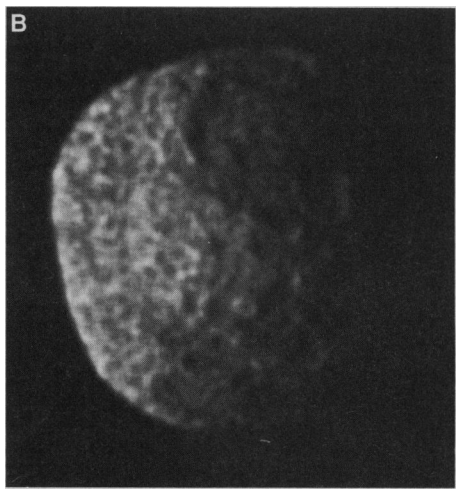

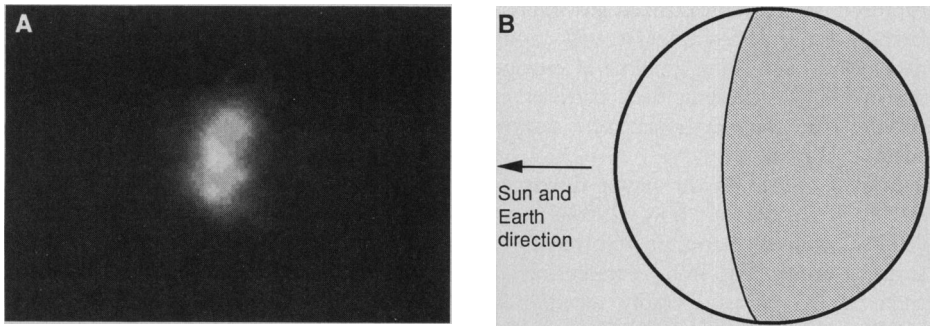

Fig. 40. Voyager 2's best view of Nereid. (**A**) Acquired from a range of 4.7 million km at a phase angle of about 90°, this image has a resolution of 43 km per pixel. (**B**) Schematic of viewing geometry.

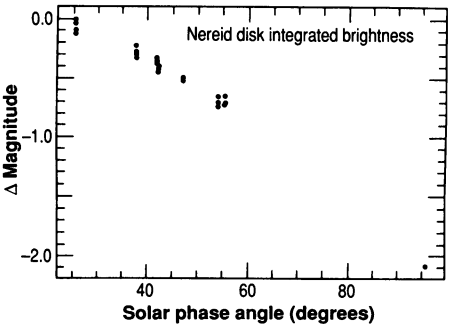

Fig. 41. Disk-integrated phase curve for Nereid. The photometric data were extracted from 15-s exposures taken through the narrow angle clear filter during the last 12 days of approach.

The present cratering rates on the satellites, estimated from methods described earlier (*76*) and from the conservative estimate of the Neptune family comet population, are given in Table 5. At Triton, the conservatively estimated present production of craters >10 km in diameter is about half the present rate on Earth (*80*) and similar to the average rate on the Moon over the last 3.3 billion years. At this rate, the craters observed on most of the sparsely cratered terrains (marked sv and sh in Fig. 31) of Triton could all have been generated in the last billion years or so.

Even at the conservatively estimated cratering rates, the small, innermost satellites 1989N5 and 1989N6 are not likely to have survived intact over the last 3.5 billion years. These satellites are probably fragments produced by catastrophic disruption of a larger body in the last 2 or so billion years, possibly even in the last half-billion years. 1989N2, 1989N3, and 1989N4, on the other hand, might have escaped destruction by comet impact at the present rate, but would almost certainly have been destroyed by collisions during an early period of heavy bombardment. The rate of cratering on these satellites by comet impact is about three to five times higher than on 1989N1; this result is independent of the estimate of the comet population. The large craters observed on 1989N1 suggest a fluence of impacting bodies that would have destroyed 1989N2, 1989N3, and 1989N4. Most likely these satellites are the product of a disruption of a body comparable in size to 1989N1 near the end of the heavy bombardment period or somewhat later. Distant Nereid appears to have been almost immune to collisional disruption by comet impact in the period since heavy bombardment.

Table 5. Estimated present cratering rates and past production of large craters on the satellites of Neptune. The entries are as follows: $P > 10$ km is the estimated present rate of production of craters >10 km diameter in units of 10 to 14. D_{max} is the diameter of the largest crater likely to have been formed in 3.5 billion years at the current rate of cratering. F_{rsat} is the frequency of production of craters with diameters larger than the radius of the satellite over a time period of 3.5 billion years. The column headed $D > R_{sat}$ gives the number of craters with diameters greater than the radius of the satellite that would have been formed while the observed craters on N1 were formed.

Satellite	Present rate			N1 equivalent	Implications for impact history
	$P > 10$ km	D_{max} (km)	F_{rsat}	$D > R_{sat}$	
Nereid	0.06	8.8	0.0015	0.01	Little modification by comet impacts in last 3.5 billion years.
Triton	0.84	193	0.014	0.1	Oldest cratered surfaces probably about 3.5 billion years old. Youngest crater surfaces probably less than 0.5 billion years old.
N1	5.7	81	0.14	1.0	Observed surface probably dates to period of heavy bombardment.
N2	16	66	0.44	3.2	These satellites probably were derived from fragmentation of a larger body near the end of heavy bombardment.
N4	21	71	0.60	4.4	
N3	29	70	0.85	6.2	
N5	41	46	1.4	10	Probably formed by fragmentation of larger parent body about 2 to 2.5 billion years ago.
N6	50	35	1.8	13	

REFERENCES AND NOTES

1. B. A. Smith *et al.*, *Science* **233**, 43 (1986).
2. B. A. Smith *et al.*, *ibid.* **204**, 951 (1979); *ibid.* **206**, 927 (1979).
3. J. W. Warwick *et al.*, *ibid.* **246**, 1498 (1989).
4. H. B. Hammel *et al.*, *ibid.* **245**, 1367 (1989).
5. B. A. Smith and G. E. Hunt, in *Jupiter*, T. Gehrels, Ed. (Univ. of Arizona Press, Tucson, 1976), pp. 564–585.
6. H. B. Hammel, *Bull. Amer. Astron. Soc.*, in press.
7. The Voyager images were processed with software that greatly reduces limb darkening or limb brightening. Specifically, a Minnaert function was used with $k = 0.7$.
8. H. B. Hammel, K. H. Baines, J. T. Bergstralh, *Icarus* **80**, 416 (1989).
9. W. H. Smith, W. V. Schempp, K. H. Baines, *Astrophys. J.* **343**, 450 (1989).
10. K. H. Baines and W. H. Smith, *Icarus*, in press.
11. J. B. Pollack *et al.*, *ibid.* **65**, 442 (1986); J. B. Pollack *et al.*, *J. Geophys. Res.* **92**, 15037 (1987).
12. K. H. Baines and J. T. Bergstralh, *Icarus* **65**, 406 (1986).
13. P. N. Romani and S. K. Atreya, *Geophys. Res. Lett.* **16**, 941 (1989).
14. G. L. Tyler *et al.*, *Science* **246**, 1466 (1989).
15. The radiative transfer model was a multilayer model based on the delta-Eddington approximation. The background atmosphere contained stratospheric aerosols, a methane cloud, and an optically thick cloud whose top was at 3 bars. Parameters were adjusted so the background model matched ground-based spectrophotometry in the visible and near infrared. A cloud layer was introduced to represent a feature; its optical depth and altitude were adjustable parameters.
16. We assumed that the product of the single-scattering albedo and phase function was independent of altitude. This product, determined from the value of the nearly constant brightness at low altitudes, was significantly greater (by a factor of 1.7) than that expected just from Rayleigh scattering, implying that scattering by stratospheric aerosols makes an important contribution to the observed brightness.
17. H. G. Solberg, *Planet. Space Sci.* **17**, 1573 (1969); L. A. Youngblood and R. F. Beebe, *Nature* **280**, 771 (1979).
18. B. A. Smith *et al.*, *Bull. Am. Astron. Soc.* **11**, 570 (1979); R. J. Terrile and B. A. Smith, *ibid.* **16**, 657 (1984); H. B. Hammel, *Icarus* **80**, 14 (1989).
19. H. B. Hammel, *Science* **244**, 1165 (1989).
20. B. Conrath *et al.*, *ibid.* **246**, 1454 (1989).
21. Another stability condition involves the potential vorticity q which is given by $(\zeta + f)/h$, where ζ is the relative vorticity (approximately $-du/dy$), u is the zonal velocity, y is the northward coordinate, f is 2

$\Omega\sin\varphi$, and h is the thickness (mass per unit area) of the atmospheric layer. A zonal flow is stable when the latitudinal gradient of q is positive everywhere. Although we do not know ζ accurately, $(\zeta + f)$ is likely to vary as f, which is proportional to $\sin\varphi$. Thus, $|\zeta + f|$ is large at the poles and zero at the equator. Because the interior of Neptune rotates faster than the atmosphere at most latitudes, the pressure surfaces become more oblate with increasing depth below the cloud tops. This means that the thickness h of the layer just below the cloud tops is also large at the poles and small at the equator. The potential vorticity $q = (\zeta + f)/h$ might then be nearly constant in each hemisphere, merely changing sign at the equator. A constant-potential-vorticity atmosphere is marginally stable and is diagnostic of horizontal mixing [P. S. Marcus, *Nature* **331**, 693 (1988); T. E. Dowling and A. P. Ingersoll, *J. Atmos. Sci.*, in press].

22. H. J. Reitsema *et al.*, *Science* **215**, 289 (1982); C. E. Couvault *et al.*, *Icarus* **67**, 126 (1986); W. B. Hubbard *et al.*, *Nature* **319**, 636 (1986); P. D. Nicholson *et al.*, in preparation.
23. B. A. Smith *et al.*, *Science* **212**, 163 (1981); B. A. Smith *et al.*, *ibid.* **215**, 504 (1982); J. N. Cuzzi *et al.*, in *Planetary Rings*, R. Greenberg and A. Brahic, Eds. (Univ. of Arizona Press, Tucson, 1984), pp. 73–199.
24. A. L. Lane *et al.*, *Science* **233**, 65 (1986); J. Colwell *et al.*, *Icarus*, in press.
25. P. Goldreich and S. Tremaine, *Annu. Rev. Astron. Astrophys.* **20**, 249 (1982); T. G. Northrop and J. E. P. Connerney, *Icarus* **70**, 124 (1987); L. R. Doyle *et al.*, *ibid.* **80**, 104 (1989); J. N. Cuzzi and R. H. Durisen, *ibid.*, in press; L. W. Esposito and J. E. Colwell, *Nature* **339**, 605 (1989).
26. J. J. Lissauer, *Nature* **318**, 544 (1985).
27. P. Goldreich, S. Tremaine, N. Borderies, *Astron. J.* **92**, 490 (1986).
28. A. R. Dobrovolskis, *Icarus* **43**, 222 (1980); N. Borderies, *ibid.* **77**, 135 (1989); A. Dobrovolskis, in preparation.
29. A. L. Lane *et al.*, *Science* **246**, 1450 (1989).
30. Two sets of images were included in the search, yielding nearly full azimuthal coverage from an orbital radius of 34,000 km to 65,000 km, with partial coverage out to 90,000 km. The first set consisted of 94 narrow angle images, taken with 61-s exposures and resolutions that varied from 76 to 88 km per line pair. The second set had 40 narrow angle images, taken with an exposure of 15 s and a resolution of 37 km per line pair. For a point source, the change in resolution for the second set of data nearly compensates for the reduced exposure time. This results in both sets yielding virtually the same limit of detectability.
31. M. Ockert *et al.*, *J. Geophys. Res.* **92**, 14969 (1987); L. R. Doyle *et al.*, *Icarus* **80**, 104 (1989); H. C. Dones, thesis, University of California, Berkeley, 1989.
32. M. Ockert *et al.*, *Bull. Amer. Astron. Soc.* **20**, 854 (1988); M. Showalter and J. Cuzzi, *ibid.*, p. 855.
33. The equivalent width is defined as $E = \int(I/F)dr = [4\omega_0 P(\alpha)/\cos\theta]\int\tau dr$, where (if the incident solar flux is πF) I/F is the ring reflectivity, equaling unity for a perfectly reflecting Lambert disk illuminated and viewed at normal incidence. The I/F is defined in terms of the particle single scattering albedo ω_0 and phase function $P(\alpha)$, the viewing angle from the ring normal θ, and the ring normal optical depth τ. The quantity $\int\tau dr$ is often referred to as the equivalent depth. The optical depth and equivalent depth used here may differ by a factor of two from those determined from ground-based stellar occultation measurements because of diffraction corrections. [For further discussion, see J. Cuzzi *et al.*, in *Planetary Rings*, R. Greenberg and A. Brahic, Eds. (Univ. of Arizona Press, Tucson, 1984) pp. 73–199; and R. G. French *et al.*, in *Uranus*, J. Bergstralh and M. S. Matthews, Eds. (Univ. of Arizona Press, Tucson, 1989), in press.]
34. N. Divine and P. Nicholson, private communication.
35. P. Nicholson *et al.*, in preparation.
36. S. Dermott *et al.*, *Nature* **284**, 309 (1980); A. Dobrovolskis, in preparation.
37. A. W. Harris, in *Planetary Rings*, R. Greenberg and A. Brahic, Eds. (Univ. of Arizona Press, Tucson, 1984), pp. 641–659.
38. P. Thomas, C. Weitz, J. Veverka, *Icarus* **81**, 92 (1989).
39. Compare Table 5; Table 3 of B. A. Smith *et al.*, *Science* **233**, 43 (1986); Table 2 of B. A. Smith *et al.*, *ibid.* **215**, 504 (1982).
40. J. A. Burns *et al.*, *Icarus* **44**, 339 (1980); J. A. Burns *et al.*, in *Planetary Rings*, R. Greenberg and A. Brahic, Eds. (Univ. of Arizona Press, Tucson, 1984), pp. 200–272.
41. A. L. Broadfoot *et al.*, *Science* **233**, 74 (1986).
42. W.-H. Ip, *Icarus* **60**, 547 (1984); J. N. Cuzzi and R. H. Durisen, *ibid.*, in press.
43. J. N. Cuzzi and J. A. Burns, *ibid.* **74**, 284 (1988); J. E. Colwell and L. E. Esposito, in preparation.
44. L. W. Esposito and J. E. Colwell, *Nature* **339**, 605 (1989); J. E. Colwell and L. W. Esposito, in preparation.
45. C. C. Porco and P. Goldreich, *Astron. J.* **93**, 724 (1987); R. French *et al.*, in *Uranus*, J. Bergstralh and M. S. Matthews, Eds. (Univ. Arizona Press, Tucson, 1989), in press.
46. D. N. C. Lin *et al.*, *Mon. Not. Roy. Astron. Soc.* **227**, 75 (1987); P. Goldreich, private communication.
47. M. S. Marley, W. B. Hubbard, C. C. Porco, *Bull. Amer. Astron. Soc.* **21**, 913 (1989).
48. B. A. Smith, in *Uranus and Neptune NASA CP-2330*, J. T. Bergstralh, Ed. (National Aeronautics and Space Administration, Washington, DC, 1984), pp. 213–223.
49. D. P. Cruikshank and R. H. Brown, in *Satellites*, J. A. Burns and M. S. Matthews, Eds. (Univ. of Ariz. Press, Tucson, 1986), pp. 836–873.
50. D. P. Cruikshank, R. H. Brown, R. N. Clark, *Icarus* **58**, 293 (1984); D. P. Cruikshank, R. H. Brown, L. P. Giver, A. T. Tokunaga, *Science* **245**, 283 (1989).
51. R. H. Brown, T. V. Johnson, J. B. Pollack, in *Uranus*, J. T. Bergstralh and M. S. Matthews, Eds. (Univ. of Ariz. Press, Tucson, in press).
52. D. J. Tholen and M. W. Buie, *Bull. Amer. Astron. Soc.* **20**, 807 (1988).
53. T. V. Johnson, R. H. Brown, J. B. Pollack, *J. Geophys. Res.* **92**, 14884 (1987); W. B. McKinnon and S. Mueller, *Geophys. Res. Lett.* **16**, 591 (1989); D. P. Simonelli and J. B. Pollack, *Icarus*, in press.
54. M. J. Lupo, *Icarus* **52**, 40 (1982).
55. J. B. Pollack, J. A. Burns, M. E. Tauber, *ibid.* **37**, 587 (1979); W. B. McKinnon and A. C. Leith, *ibid.*, in press.
56. P. Goldreich, N. Murray, P. Y. Longaretti, D. Banfield, *Science* **245**, 500 (1989).
57. E. Anders and N. Grevesse, *Geochem. Cosmochimica Acta* **53**, 197 (1989).
58. D. G. Jankowski, C. F. Chyba, P. D. Nicholson, *Icarus* **80**, 211 (1989).
59. O. G. Franz, *ibid.* **45**, 602 (1981).
60. J. Goguen, H. B. Hammel, R. H. Brown, *ibid.* **77**, 239 (1989).
61. B. J. Hapke, *J. Geophys. Res.* **86**, 3039 (1981); *Icarus* **59**, 41 (1984); *ibid.* **67**, 264 (1986). A nonlinear, least-squares approach was used to obtain best-fit Hapke parameters [P. Helfenstein, *ibid.* (in press)] $\bar{\theta}$(violet) = 3°; w(green) = 0.996. It should also be noted that the Voyager data indicate that Triton's surface is photometrically heterogeneous and these represent global averages.
62. B. Buratti, *Icarus* **61**, 208 (1985).
63. A. Verbiscer and J. Veverka, *Bull. Amer. Astron. Soc.* **20**, 872 (1988).
64. D. J. Tholen, personal communication.
65. J. F. Bell, R. N. Clark, T. B. McCord, D. P. Cruikshank, *Bull. Amer. Astron. Soc.* **11**, 570 (1979).
66. D. P. Cruikshank, A. Stockton, H. M. Dyck, E. E. Becklin, W. Macy, *Icarus* **40**, 104 (1979).
67. L. M. Trafton, in *Uranus and Neptune NASA CP-2330*, J. T. Bergstralh, Ed. (National Aeronautics and Space Administration, Washington, DC, 1984), pp. 481–496.
68. L. Broadfoot *et al.*, *Science* **246**, 1459 (1989).
69. W. R. Thompson, B. Murray, B. N. Khare, C. Sagan, *J. Geophys. Res.* **92**, 14933 (1987); L. J. Lanzerotti and W. L. Brown, in Proceedings of the NATO Advanced Research Workshop on Ices in the Solar System, Nice, France (1984); G. Strazzulla, L. Calcagno, G. Foti, *Mon. Nat. Roy. Astron. Soc.* **204**, 59 (1983).
70. J. S. Kargel and S. K. Croft, *Lunar Planet. Sci. Conf.* **XX**, 500 (1989); D. G. Jankowski and S. W. Squyres, *Science* **241**, 1322 (1989); D. J. Stevenson and J. I. Lunine, *Nature* **323**, 46 (1986).
71. S. K. Croft and L. A. Soderblom, in *Uranus*, J. T. Bergstralh and M. S. Matthews, Eds. (Univ. of Ariz. Press, Tucson, in press).
72. C. P. McKay, J. B. Pollack, A. P. Zent, D. P. Cruikshank, R. Courtin, *Geophys. Res. Lett.* **16**, 973 (1989).
73. J. B. Pollack and J. N. Cuzzi, *J. Atmos. Sci.* **37**, 868 (1980); K. N. Liou, Q. Cai, J. B. Pollack, J. N. Cuzzi, *Appl. Opt.* **22**, 3001 (1983).
74. M. W. Schaefer and B. E. Schaefer, *Nature* **333**, 436 (1988).
75. T. V. Johnson and T. R. McGetchin, *Icarus* **18**, 612 (1973).
76. E. M. Shoemaker and R. F. Wolfe, in *Satellites of Jupiter*, D. Morrison, Ed. (Univ. of Ariz. Press, Tucson, 1982), pp. 277–339.
77. ———, C. S. Shoemaker, *Lunar Planet. Sci. Conf.* **XVII**, 799 (1986).
78. E. Everhart, *Astrophys. J.* **10**, L131 (1972); E. Everhart, in *Comets-Asteroids-Meteorites*, A. H. Delsemme, Ed. (Univ. of Toledo Press, Toledo, 1977), pp. 99–104.
79. M. Duncan, T. Quinn, S. Tremaine, *Astrophys. J.* **328**, L169 (1988); M. Duncan, T. Quinn, S. Tremaine, *Icarus*, in press.
80. E. M. Shoemaker, C. S. Shoemaker, R. F. Wolfe, in *Global Catastrophes in Earth History*, Lunar and Planetary Science Institute Cont. **673**, 174 (1988).
81. We gratefully acknowledge the skill, hard work, and good cheer of all our colleagues who helped us during this final Voyager encounter, especially the Voyager Spacecraft Team, for providing us with a healthy, reliable, obedient, and stable spacecraft with which to perform our imaging experiments. Special thanks go to H. Marderness, G. Hanover, and E. Wahl for designing the image motion compensation; G. Masters, M. Urban, B. Cunningham, and D. Rice for extended exposure capability; and our own E. Simien for making every image available. We thank our fellow scientists J. Burns, C. Ferrari, D. M. Janes, F. Rocques, and the analysts at MIPL, coordinated and directed by C. Avis and S. Lavoie: G. Garneau, H. Mortensen, C. Stanley, L. Wynn, L. Wainio, G. Yagi, D. Alexander, C. Levine, E. Runkle, J. Yoshimizu, R. Mortensen, and D. Jensen. We thank those at the USGS in Flagstaff for their help: K. Edwards, E. Eliason, T. Becker, J. Swann, K. Hoyt, R. Batson, J. Inge, P. Bridges, and H. Morgan. We also thank P. Goldreich, P. Nicholson, D. Stevenson, and R. West for careful and thoughtful reviews of this manuscript.

6 November 1989; accepted 15 November 1989